Crystallization of late-stage MORB under varying water activities and redox conditions: Implications for the formation of highly evolved lavas and oxide gabbro in the ocean crust

J. Koepke [a,*], R.E. Botcharnikov [a,b], J.H. Natland [c]

[a] Institute for Mineralogy, Leibniz Universitä Hannover, Callinstr. 3, D-30167 Hannover, Germany
[b] Institut für Geowissenschaften, Johannes Gutenberg Universität Mainz, J-J-Becher-Weg 21, D-55128 Mainz, Germany
[c] Rosenstiel School of Marine and Atmospheric Science, University of Miami, Miami, FL 33149, USA

ARTICLE INFO

ABSTRACT

In order to understand late magmatic processes that occur in the deep oceanic crust, we performed a phase-equilibria study in a representative late-stage system at a pressure of 200 MPa with a special focus on the role of water and oxygen fugacity. The starting composition for the experiments was evaluated based on a statistical approach using evolved fresh MORB glasses from the database PETDB highest in FeO and TiO_2 (in average 17.92 wt% and 3.73 wt%, respectively), assumed to represent frozen liquids erupted at the seafloor generated by extensive differentiation of MORB.

We conducted crystallization experiments in a range of temperatures from 850 to 1050 °C with water activities from 0.1 to 1 and under redox conditions from FMQ-1.1 to FMQ + 3.2 (FMQ = fayalite-magnetite-quartz oxygen buffer). The results show that in this Fe- and Ti-rich late-stage system, Fe-Ti-oxides are the liquidus phases followed by clinopyroxene, apatite, and plagioclase, which is more stable at low water activity. Amphibole is stable at high aH₂O and at temperatures lower than 900 °C. The evolution of the melt composition with decreasing temperature and aH₂O follows in general the liquid lines of descent observed in other experiments in ferrobasaltic compositions. Orthopyroxene, which occurs as late crystallizing phase in many oceanic gabbros, was absent among the experimental mineral assemblages. Based on the evolution of coexisting clinopyroxene and plagioclase compositions, our experiments define a trend similar to the trends from other suites of oceanic gabbros from various locations.

Our experimental results shed new light on the formation of highly evolved lavas from fast- and intermediate spreading mid-ocean ridges implying a relatively simple two-step differentiation model. First, primitive MORBs differentiate along the 1 atm cotectic trend to typical ferrobasaltic compositions by fractionation of olivine, plagioclase, clinopyroxene. This trend continues as long as Fe-Ti oxides are not saturated, which is strongly dependent on the prevailing oxygen fugacity. When such ferrobasaltic magmas are cut off from replenishment by fresh MORB, the possibility for further differentiation to highly evolved melts is given by fractionation of oxides, clinopyroxene, plagioclase, apatite and finally amphibole and apatite. Phase relations obtained in our experiments help to understand the formation of oxide gabbros from the ultra-slow spreading Southwest Indian Ridge (IODP drill core Hole 735B). The experimental evaluated crystallization order with temperature is in accord with the record of crystallization of the Hole 735B oxide gabbros.

© 2018 Elsevier B.V. All rights reserved.

1. Introduction

The basic processes responsible for the generation of oceanic crust are ascent and differentiation/solidification of Mid Ocean Ridge Basalts (MORB). After the main stage of cotectic crystallization in MORB magmas with the characteristic phase assemblage olivine–plagioclase–clinopyroxene, the solidification of the MORB magma at depth may continue, resulting in the precipitation of late-stage minerals like Fe-Ti oxides, amphibole, orthopyroxene, sulfides, apatite, and zircon, often observable in oceanic gabbros. They are typically arranged in interstitial assemblages between the primary minerals and are produced either by cotectic crystallization or by peritectic reactions.

The best example illustrating the textural and compositional relationships between the late stage minerals is the gabbro section drilled in the framework of the International Ocean Discovery Program (IODP) at Site 735 and 1105A within the Atlantis Bank at the Southwest

* Corresponding author.
E-mail address: Koepke@mineralogie.uni-hannover.de (J. Koepke).

Indian Ridge (SWIR). Recently, Atlantis Bank at the SWIR was again the target of an IODP expedition (Expedition 360 at Site U1473; MacLeod et al., 2017). Detailed results such as mineral analyses related to the new expedition are not published yet, so that we focus here mainly on the results of the drill cores from Hole 735B.

Due to the very high amount of oxides and other late-stage minerals, these gabbros can be used to get a better understanding of the general late-stage processes in oceanic gabbros. For instance, for Hole 735B about 75% of the drilled section represent products of the main stage crystallization, whereas 25% involve later, crosscutting, and usually more deformed oxide gabbros (e.g., Dick et al., 2000). During the late magmatic stage, highly differentiated, iron-titanium–rich melts percolated through the gabbroic pile, leading to the precipitation of typical late-stage minerals like intergrowths of ilmenite and magnetite, titanian brown amphibole, orthopyroxene, and sulfide, especially in shear zones and fractures (Natland et al., 1991; Natland and Dick, 2001, 2002; Ozawa et al., 1991). Based on the bulk rock geochemistry, the gabbroic rocks recovered in the 1508 m deep Hole 735B can be separated into five units, with thicknesses varying from 200 to 600 m. These are each characterized by an upward trend of decreasing Mg# (MgO/{MgO + FeO}, on a molar basis), with a sharp increase in Mg# at the beginning of each overlying unit (see Fig. 2 in Dick et al., 2000). These chemical units defined by these trends partially overlap and each is characterized by several smaller petrographically distinct intrusive intervals.

A striking feature of these rocks is the presence of very oxide-rich gabbro (oxide gabbro or ferrogabbro), occurring both in hundreds of narrow seams (several to tens of cm thick) and in one interval of about 70-m thickness. For many authors, these rocks represent the products of some kind of fractional crystallization from an evolved iron-rich melt (e.g., Natland and Dick, 2002). This is indicated because the oxide gabbros contain substantially more sodic plagioclase and more iron-rich pyroxenes and olivine (Dick et al., 2000; Natland and Dick, 2002; Ozawa et al., 1991) than typical olivine gabbros. In addition, they often contain significant quantities of orthopyroxene, brown amphibole and sometimes pigeonite (Ozawa et al., 1991).

Dick et al. (2000) and Natland and Dick (2001) suggested that the complex intrusive relations between gabbros of different state of differentiation in mutual contact were triggered by tectonic processes and do not represent the result of an in-situ upward differentiation of a large magma body.

Moreover, many oxide gabbros from the Atlantis Bank drill cores are closely related to SiO_2-rich rocks or so-called "felsic veins" (e.g., Dick et al., 2000; MacLeod et al., 2017) that have the compositions of typical oceanic plagiogranites (for definition of this term see Koepke et al., 2007; technically, they are quartz diorites, tonalites, trondhjemites and rare granodiorites). The intimate association between rocks derived from Fe-Ti-rich and silicic melts implies for some authors that silicate

liquid immiscibility may have proceeded deep in the SWIR crust (Natland et al., 1991), based on the experimental study of Dixon and Rutherford (1979), a model not yet verified.

Up to now, no detail experimental data exist on the stability and phase relations of Fe-Ti oxides, amphibole, and sulfides, the ubiquitous late-stage phases in typical oceanic gabbros, as a function of temperature, aH_2O, and fO_2. Due to the omnipresence of amphibole in the natural late stage assemblages, it is obvious that the activity of water is of particular significance. The existing experimental data of Toplis and Carroll (1995) on evolved ferrobasaltic melts (their "SC4" starting composition is very similar to the starting composition "LS" used in this study; see below and also Table 1), were obtained in a wide temperature range, but at atmospheric pressure and under dry conditions. Thus, a direct application of these data to the assumed hydrous late-stage processes in oceanic gabbros is hampered. Berndt et al. (2005) and Feig et al. (2006, 2010) have experimentally investigated phase equilibria in primitive MORB-type basaltic systems as a function of oxygen fugacity (fO_2) and water activity (aH_2O). The combined experimental data enable a profound insight into the main stage of crystallization processes within magma chambers at mid-ocean ridges, but are not suitable for the application to late-stage magmatic processes because the investigated systems are too primitive in composition.

An experimental study of Botcharnikov et al. (2008) for a hydrous ferrobasalt shows a dramatic effect of water on liquid lines of descent, and phase stability and mineral compositions when compared with the experimental results that both Toplis and Carroll (1995) and Thy et al. (2006) obtained in a dry ferrobasaltic system with similar starting composition. As in their studies, Fe-Ti-oxide minerals (i.e., magnetite and ilmenite-hematite) crystallize over a wide range of temperatures, redox conditions and water activities. The important observation is the appearance of amphibole as a late mineral phase at temperatures <1000 °C at high water activities. Furthermore, it was observed that water activity has an effect on the stability of silicate minerals but no effect on the stability of Fe-Ti oxides. Similar observations were also recorded by Sisson and Grove (1993) in an experimental phase equilibria study on hydrous high-alumina basalts, who reported that water depresses the appearance temperatures of crystalline silicates, but has lesser effect on titano-magnetite. However, what all studies have in common is that neither orthopyroxene nor pigeonite, which are also typical phases present in late-stage assemblages of natural oceanic gabbros, were found both in dry (Toplis and Carroll, 1995) or in hydrous (Botcharnikov et al., 2008) ferrobasaltic experimental series.

This experimental study is focused on the phase equilibria in a typical MORB late-stage system for the application to the late-stage evolution of oceanic gabbros and to highly evolved abyssal lavas. In order to correspond to the natural processes as close as possible, volatiles such as H_2O (presence of amphibole in the natural paragenesis of oceanic

Table 1
Compositions of the experimental late-stage system "LS" and of other tholeiitic systems.

	SiO_2	TiO_2	Al_2O_3	FeO^t	MnO	MgO	CaO	Na_2O	K_2O	P_2O_5	S (ppm)	Total	norm. ol	norm. qz
LS evalu.[a]	50.10	3.64	11.58	17.71	0.29	4.04	8.94	2.73	0.26	0.40	2200	99.69		1.84
1 sigma	1.00	0.25	0.57	0.63	0.03	0.42	0.47	0.28	0.12	0.10				
LS synth.[b]	49.56	3.73	11.42	17.92	0.31	3.89	8.93	2.85	0.28	0.65		99.66		1.40
1 sigma	0.33	0.08	0.15	0.33	0.11	0.14	0.22	0.20	0.04	0.10				
MORB[c]	49.64	0.87	16.07	8.63	0.15	9.77	12.44	2.28	0.08	0.08		100.00	14.98	
735B[d]	43.50	4.50	11.29	21.33	0.33	7.66	6.98	2.74	0.06	0.07		98.46	29.80	
SC1[e]	48.70	2.90	14.90	13.10		6.50	10.90	2.70	0.30			100.00	12.12	
1256D[f]	49.58	4.12	12.15	17.44	0.17	4.45	7.96	3.68	0.23	0.22		100.00	7.93	

FeO^t – Fe total as FeO; "norm. ol" and "norm. qz" represent the normative olivine and quartz values.

[a] Evaluated starting composition representing a MORB late-stage system. Average of 69 ferrobasaltic MORB glasses out of the PETDB data base; see text for details.

[b] Composition of the synthesized starting material "LS" used in this study (average of 15 analyses).

[c] Primitive MORB (starting composition of Berndt et al., 2005; normalized to 100%).

[d] Average Hole 735B oxide gabbronorite of Dick et al. (2000).

[e] Starting composition of Toplis and Carroll (1995). Assumed parental composition of the Skaergaard 5) Layered Intrusion (Greenland) according to Brooks and Nielsen (1978); normalized to 100%. A very similar composition was used as starting material from Botcharnikov et al. (2008).

[f] Quartz-rich oxide gabbro drilled by IODP at Site 1256, interpreted as frozen Fe-Ti-rich late-stage melt (Expedition 312, core 212, Section 1, 29–32 cm).

gabbros), sulfur (presence of sulfides), and P_2O_5 (presence of apatite) were included in the experimental system named "LS" (see below). Since the differentiation in such an iron-rich system is strongly controlled by the stability of oxides which is in turn a function of oxygen fugacity, we varied fO_2 in our experimental series in a wide range between $\log fO_2 \sim FMQ-1.1$ and $\sim FMQ + 3.2$.

2. Starting composition

For evaluating the composition of the experimental MORB-type late stage system, we chose a statistical approach. It is problematic to obtain a proper composition directly from oxide gabbros of the IODP cores drilled at SWIR, because it is obvious that oxide gabbros (as well as more primitive gabbros) do not represent simple frozen melts but instead are cumulates or mixtures of cumulates and frozen melts. An inspection of the analyses of SWIR oxide gabbros (Dick et al., 1999; 2000; Robinson et al., 1991) reveals that these Fe-Ti-rich rocks (Fig. 1a; see also Table 1) are in general too poor in SiO_2 (Fig. 1b) for representing true residual liquids when compared with corresponding fresh glasses from differentiated MORB as discussed below. This implies that the SWIR oxide gabbros generally lost some amount of melt by compaction or adcumulus growth, which was obviously enriched in SiO_2. The cumulus origin is also supported by a large scatter in P_2O_5 when plotted against TiO_2 (Fig. 1c indicates the presence or absence of cumulate apatite), and by in general too low K_2O contents at high TiO_2 concentrations (Fig. 1d). Natland et al. (1991) described this in terms of very low Zr contents and on this basis estimated residual melt porosities of only a few percent for most gabbros of Hole 735B.

Therefore, we evaluated the composition of a typical "late stage" experimental system, hereafter termed "LS", following an approach where fresh Fe-Ti-rich glasses (regarded as frozen liquids) from mid-ocean ridges, were considered to be generated by advanced MORB differentiation. In this approach, we used analyses fresh MORB glasses from the database "PETDB" (Lehnert et al., 2000) representing rocks from ocean ridges all over the world including all glasses from "normal" spreading centers. MORB differentiation follows a typical tholeiitic evolution trend (e.g., Miyashiro, 1974), which is characterized by initial Fe-Ti enrichment ("ferrobasaltic trend") followed by a Fe-Ti depletion coupled with SiO_2 enrichment. The rationale behind this is that before the kink point, the liquids are not saturated in Fe-Ti oxides, thus still need some development to become saturated in Fe-Ti oxides. After the onset of oxide crystallization, which can be the result of increasing oxygen fugacity (e.g., Berndt et al., 2005; Botcharnikov et al., 2008; Toplis and Carroll, 1995) or water activity (e.g., Botcharnikov et al., 2008; Sisson and Grove, 1993), FeO and TiO_2 concentrations in the liquids drop and the liquids start to become enriched in silica. Fig. 1 shows compositional plots for fresh MORB glasses obtained from the data base PETDB as well as oxide gabbros from SWIR, where TiO_2 is regarded as parameter of differentiation. Fig. 1a shows a good correlation between FeO^t (total iron as FeO) and TiO_2, leading to very Fe- and Ti-rich compositions at the advanced ferrobasaltic stage of differentiation. The very high FeO and TiO_2 concentrations at this point are assumed to represent these highly differentiated late-stage liquids, and that these are similar to those that percolate through the gabbroic cumulus pile in the deep ocean crust resulting in pervasive precipitation of Fe-Ti-rich late-stage parageneses. During the ferrobasaltic portion of differentiation, SiO_2 concentration is more or less constant (Fig. 1b), but in fact some SiO_2 enrichment occurs on a molar basis. The ferrobasaltic evolution trend defined by natural MORB is also confirmed by 1 atm experimental studies using natural primitive MORB from mid-ocean ridges as starting material (e.g., Dixon and Rutherford, 1979; Juster et al., 1989; Tormey et al., 1987; Walker et al., 1979). The melt compositions of these studies show a homogeneous trend with enrichment of FeO and TiO_2, overlapping with the trend of the natural MORBs
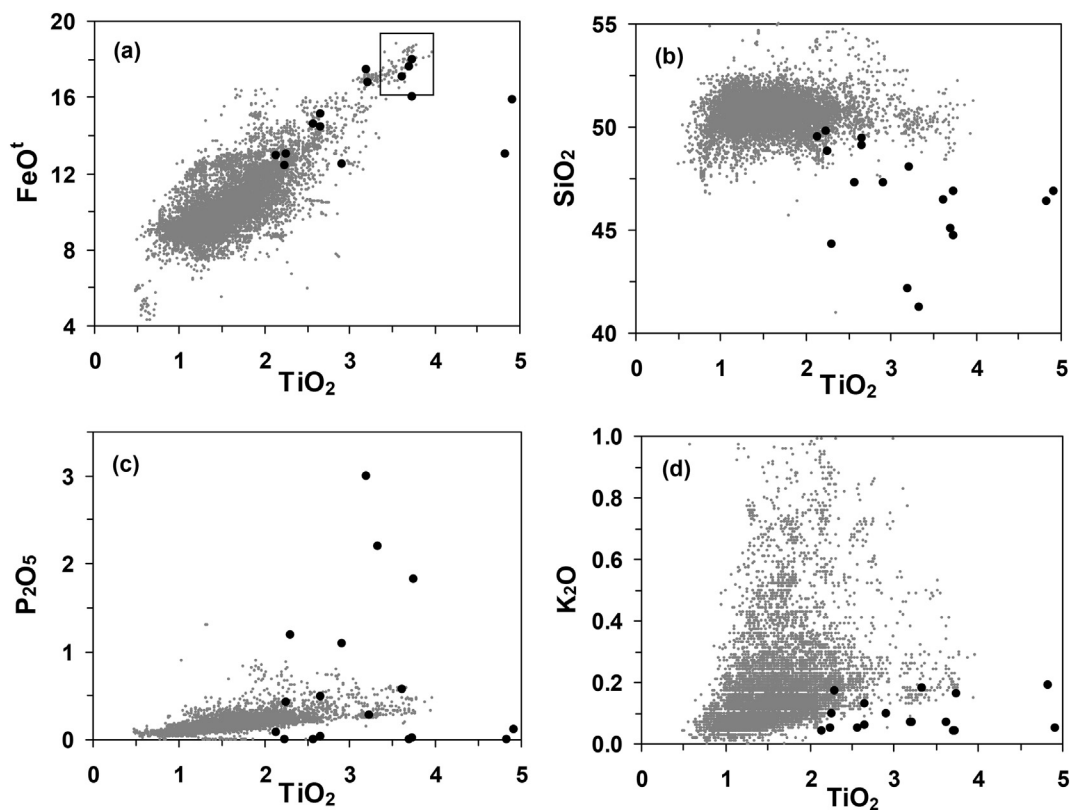

Fig. 1. FeO^t (total iron as FeO), SiO_2, P_2O_5, K_2O versus TiO_2 diagrams (wt%) for fresh MORB glasses from ridges of world's oceans and for oxide gabbros from Leg 118/176 at SWIR (black circles). The MORB glasses (grey dots; more than 14,000 datasets) are from the PETDB database (Lehnert et al., 2000) and are regarded as frozen liquids from diverse stages of MORB differentiation. The year of evaluation was 2006. For details see text.

shown in Fig. 1. With differentiation to ferrobasaltic composition, incompatible elements such as P and K are systematically enriched in the melt (Fig. 1c, d). Those compositions of interest that can be regarded as representative of a MORB late-stage system for our experimental study, lie "at the end" of the ferrobasaltic trend and have high amounts of FeO (~ 18 wt%) and TiO_2 (3.5–4 wt%) as marked in Fig. 1a. This part of Fig. 1a is enlarged in Fig. 2a, in which values with TiO_2 > 3.4 wt% are displayed. For evaluating a typical late-stage composition as starting composition ("LS") for our experiments, an average composition using all analyses with TiO_2 > 3.4 wt% was calculated (69 analyses; TiO_2 value arbitrarily chosen; Fig. 2; Table 1). As expected, our starting system LS falls exactly on the liquid lines of descent of those 1-atm experimental studies using natural primitive MORB as starting material (see also Section 4.2, glass compositions).

Since only two analyses out of the 69 selected datasets included sulfur concentrations, it was not possible to obtain a reasonable average sulfur content for our starting composition LS. Therefore, we estimated sulfur contents by S versus TiO_2 and S versus FeO^t relations for the whole PETDB data set for MORB glasses from diverse mid-ocean ridges (see Fig. 1). In Fig. 3, all data are displayed for which S contents are available (~ 600 data sets). With the help of linear regression, the S content for the composition LS (TiO_2 = 3.6 wt%, FeO^t = 17.7 wt%; Table 1) was calculated to be about 2200 ppm (the use of both TiO_2 and FeO^t values reveal the same S concentration).

The composition LS is listed in Table 1, together with other compositions of tholeiitic systems for comparison: a typical composition of primitive MORB (Berndt et al., 2005); an average Hole 735B oxide gabbronorite (Dick et al., 2000); a ferrobasalt (SC1) assumed to be a parental melt for the Skaergaard Layered Intrusion and investigated in the studies of Toplis and Carroll (1995) and Botcharnikov et al. (2008); a composition (SC4) of evolved SC1 ferrobasalt after ~40% of crystallization as reported by Toplis and Carroll (1995); a quartz-rich oxide diorite drilled by IODP at Site 1256 in the equatorial Pacific (Teagle et al., 2006); and the most TiO_2-rich analyses among glasses for the SWIR – AIIFZs 5–5 (Natland et al., 1991). The composition LS is quartz-normative, whereas all other compositions are olivine-normative. A comparison with the average Hole 735B oxide gabbronorite in Table 1 reveals a strong cumulus aspect for the gabbronorites, indicated by the extremely low contents of SiO_2, P_2O_5, and K_2O.

It is interesting that the chosen composition is very similar to the composition of a quartz-rich oxide diorite obtained by IODP Expedition 312 in the East Pacific Rise at Site 1256, where a continuous section of fast-spread oceanic crust from the lavas through the sheeted dikes into the uppermost gabbros was drilled (Teagle et al., 2006). This rock forms a small dike that intrudes the top of the gabbro section, and obviously represents the plutonic equivalent of a highly evolved Fe-Ti-enriched late-stage melt (Teagle et al., 2006). The close similarity of this composition with our starting material LS (Table 1) demonstrates that the chosen chemical system at least does exist in MORB magma chambers as a very late melt percolating in the deep oceanic crust, and that our experimental approach seems well-suited to elucidate the end of differentiation within MORB magma chambers. In addition, our starting composition LS is very close to the synthetic composition SC4 relevant to the Skaergaard Layered intrusion, which was experimentally investigated at atmospheric pressure by Toplis and Carroll (1995) providing a reference dataset for a dry system.

The starting glass powder of LS composition was prepared from mixtures of oxides (SiO_2, TiO_2, Al_2O_3, Fe_2O_3, MgO) and carbonates ($CaCO_3$, Na_2CO_3, K_2CO_3) ground in a rotary mortar. After 2 h of melting in a Pt crucible at 1600 °C, 1 atm, and at a log $fO_2 = -0.68$ (air), the resulting melt was quenched by dropping in water and the obtained glass was ground in an agate mortar. The powdered glass was melted a second
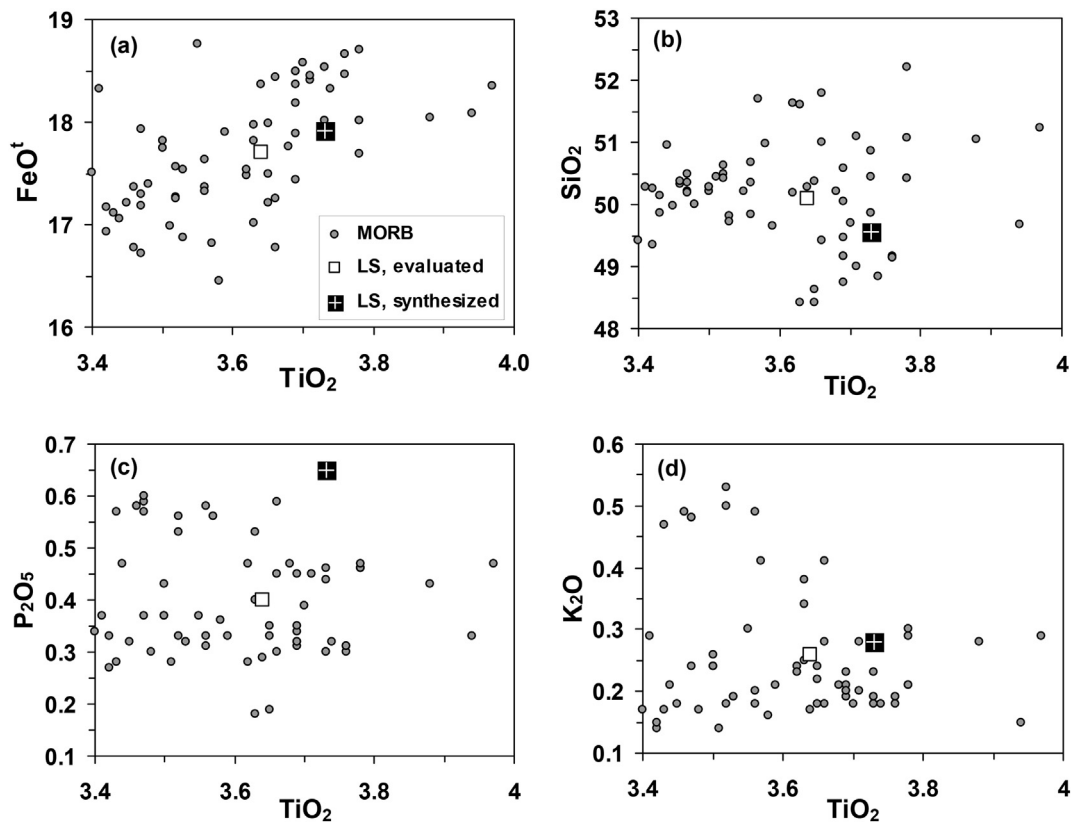
Fig. 2. FeO^t, SiO_2, P_2O_5, K_2O versus TiO_2 diagrams (wt%) for MORB glasses from world's ocean ridges with ferrobasaltic compositions representing the "end" of the ferrobasaltic trend as marked in Fig.1 a. Displayed are values with FeO^t > 16 wt% and TiO_2 > 3.4 wt% (167 data sets). For evaluating a typical late-stage composition as starting composition for our experiments ("LS"), an average using all analyses with TiO_2 > 3.4 wt% was calculated (open square). The FeO^t, SiO_2, P_2O_5, K_2O concentrations in synthesized LS composition are shown as crossed black squares (see also Table 1).
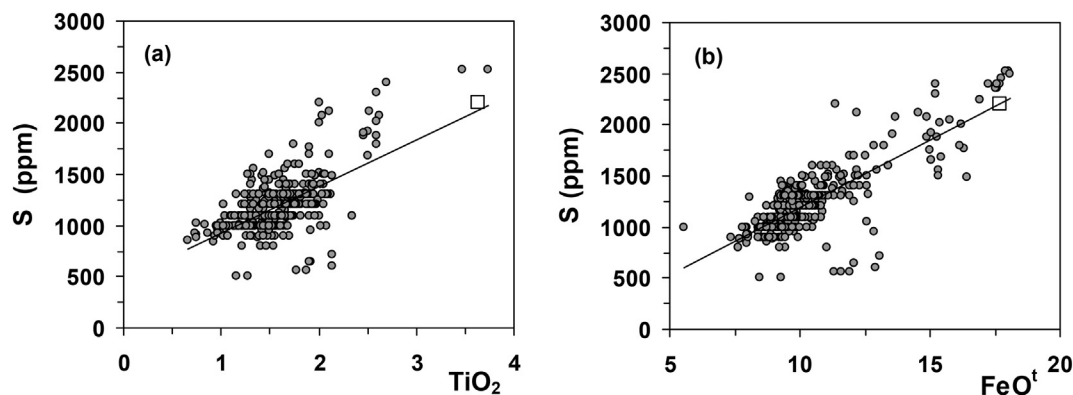
Fig. 3. Sulfur versus TiO_2 and FeO^t diagram, for evaluation of the S content in late-stage composition ("LS"). The compilation is based on the PETDB dataset for MORB glasses from diverse mid-ocean ridges (see Fig. 1). All data are displayed for which S contents are available (~ 600 datasets). With the help of linear regression, the S content for the composition "LS" was calculated to be about 2200 ppm (see text for details). The regression equation for TiO_2 is "y = 457.85x + 464.84" ($R^2 = 0.387$) and for FeO is "y = 131.98x - 128.89" ($R^2 = 0.6284$).

time for 0.5 h to get a homogeneous composition. The homogeneity of the silicate glass was verified by electron microprobe (see standard deviation of multiple analyses in Table 1).

3. Experimental approach and analytics

3.1. Experimental technique

For each experiment, about 50 mg of dry glass powder (<200 μm grain size) prepared as above was loaded into 15 mm long (inner diameter of 2.6 mm) Au capsules. All experiments were fluid-saturated and in order to simulate different fluid compositions and water activity in the system, the fluid phase in our experiments was consisted of H_2O and CO_2 added in different proportions. Silver oxalate ($Ag_2C_2O_4$) was used as a source of CO_2. Zero to 5 μl of water and a certain amount of silver oxalate (0 to 10 mg) were added to the glass powder to adjust the desired mole fraction of water (X_{H2O}^{fl}) in the capsule. The initial mole fraction of H_2O (X^{fl}_{H2Oini}) in the fluid phase was varied from $X^{fl}_{H2Oini} = 0$ (nominally dry, pure CO_2 in the fluid) to 1 (water-saturated). In order to study the behaviour of S in late-stage melts, several capsules were charged with 0.5 wt% of elemental S. This amount of S is higher than the expected S content of natural late-stage magmas (0.22 wt%, see Section 2, "starting composition"), and guaranteed saturation of the melts in S-bearing phases. Five experiments, containing elemental S and H_2O in addition to glass were conducted under both oxidizing and reducing conditions (see below). Two additional capsules contained H_2O, S and CO_2 as volatile components (Table 2). We used Au capsules to minimize the loss of Fe from the system and to avoid the reaction of capsule material with sulfur, which is known to be a very corrosive substance for most noble metals, in particular for Pt- and Pd-bearing alloys.

Most experiments were performed in internally heated pressure vessels (IHPV) oriented vertically (see Berndt et al., 2002). The total pressure was measured and recorded continuously using digital pressure transducer with an uncertainty of about 1 MPa. The variations of pressure during the experiments were <5 MPa. Temperature was measured with four unsheathed S-type (Pt-$Pt_{90}Rh_{10}$) thermocouples to control the temperature gradient over a length of ~ 3 cm inside the vessel. Temperature oscillations were below 3–5 °C depending on the vessel and experimental run. Two series of systematic experiments were performed, one with pure Ar gas as the pressure medium, and one with a mixture of Ar and H_2 gases. In the case of the pure Ar pressure medium, the intrinsic fO_2 of the vessel was close to log fO_2 ~ FMQ + 3.2 (Schuessler et al., 2008). The Ar-H_2 gas mixture was used as pressure medium to adjust the required fH_2 in the vessel and to perform experiments at the desired redox conditions. The fH_2 prevailing in the IHPV at high P and T was controlled with a Shaw-membrane made of platinum

(Berndt et al., 2002). Hydrogen pressure was applied to maintain redox conditions corresponding to the nominal oxygen buffer at log $fO_2 = $ FMQ + 1 in the systems with water activity (aH_2O) equal to 1 at given T and P. Within the sample capsule, the fH_2 was fixed due to an in-diffusion of hydrogen, controlling the fO_2 inside the capsule through the equilibrium reaction of water formation ($H_2 + 1/2\ O_2 \leftrightarrow H_2O$). Thus, in the capsules with $aH_2O < 1$, the redox conditions were more reducing than in the experiments with $aH_2O = 1$. Since aH_2O was varied between ~0.1 and 1, the overall variation in fO_2 in all experimental series was in the range between ~FMQ-1 and ~FMQ + 3.2, thus covering the range of oxygen fugacities prevailing in natural MORB magmas (Bezos and Humler, 2005).

Several additional runs were conducted in conventional cold-sealed pressure vessels at 850 °C. The vessels were pressurized with Ar gas or with H_2O. In the former case, the oxygen fugacity is expected to be similar to the redox conditions in the IHPV, while in the experiments with H_2O-pressure medium the fH_2 was maintained at the redox conditions corresponding to Ni/NiO oxygen buffer (ca. FMQ + 0.7) at $aH_2O = 1$ by placing Ni-NiO powder into the Ni-alloy autoclaves.

Crystallization experiments were performed at 200 MPa corresponding to a pressure prevailing at the 7–10-km-deep base of the oceanic crust of typical ridges. Temperature was varied between 1050 °C (close to liquidus conditions as a function of aH_2O) and 850 °C (near-solidus) in steps of 50 °C. The run duration varied from 48 to 132 h, depending on the run temperature. After the experiments, the samples were quenched at a quench rate of about 150 °C/s, preventing formation of the quench phases. The applied run conditions and volatile ratios added to the charge are listed in Table 2.

3.2. Determination of fluid composition and calculation of water activity (aH_2O) and oxygen fugacity (fO_2) in the experiments

After the experiments, the composition of the fluid phase [mole fraction of water (X_{H2O}^{fl})], equilibrated with the silicate melt ± crystals in the capsules, was determined by a weight-loss method. After the runs, the capsules were weighed, frozen by placing them into a bath of liquid nitrogen, and then punctured with a needle. After warming at room temperature, capsules were weighed again to determine the mass of CO_2 lost by puncturing as a gas phase from the open capsule, then placed in a drying oven at 110 °C for 3 min and finally weighed to measure the mass of evaporated H_2O. The determined X_{H2O}^{fl} provides an estimate of the water activity (aH_2O) prevailing in an individual capsule during the experiment. The relationship between X_{H2O}^{fl} and aH_2O was derived from empirical model of Aranovich and Newton (1999) with fugacity coefficients from Pitzer and Sterner (1995). The calculated aH_2O values are reported in Table 2. Using the estimated aH_2O values (at fH_2 fixed by the redox conditions in IHPV), the prevailing fO_2 was

Table 2
Run conditions and phase relations in crystallization experiments at 200 MPa.

Sample	Temp., °C	Time, h	$X^{fl}H_2O$ [a]	aH_2O [b]	Log fO_2	ΔQFM	Phase assemblages [c]	r2 [d]
ΔQFM nominal = +3.2 (at aH_2O=1); P = 200 MPa								
LS9	1050	48	1.00	1.00	−6.8	3.2	GL(90.0), MT(9.1), ILM(0.1)	0.30
LS10	1050	48	0.78	0.81	−7.0	3.0	GL(91.0), MT(8.0), ILM(1.0)	0.32
LS11	1050	48	0.47	0.51	−7.4	2.6	GL, MT, ILM[e], CPX	
LS12	1050	48	0.10	0.11	−8.8	1.3	GL, MT[e], ILM[e], CPX[e], PL[e]	
LS1	1000	100	1.00	1.00	−7.6	3.2	GL(81.0), MT(5.8), ILM(8.0), CPX(5.2)	0.26
LS2	1000	100	0.76	0.79	−7.8	3.0	GL(78.3), MT(8.5), ILM(5.2), CPX(8.0)	0.22
LS3	1000	100	0.40	0.44	−8.3	2.5	GL, MT, ILM, CPX, PL[e], AP[e]	
LS4	1000	100	0.09	0.10	−9.6	1.2	GL, MT, ILM[e], CPX, PL[e], AP[e]; -CtS	
LS5	950	120	1.00	1.00	−8.4	3.2	GL(65.5), MT(6.6), ILM(11.0), CPX(16.3), AP(0.6)	0.34
LS6	950	120	0.79	0.82	−8.5	3.0	GL, MT, ILM, CPX, AP[e]	
LS7	950	120	0.35	0.38	−9.2	2.4	GL[e], MT[e], ILM[e], CPX, PL, AP[e]	
LS8	950	120	0.06	0.07	−10.7	0.9	GL[e], MT[e], ILM[e], CPX[e], PL[e], AP[e]; -CtS	
LS13	900	120	1.00	1.00	−9.2	3.2	GL(50), MT(7), ILM(12), CPX(21), PL(9), AP(1)	1.54
LS14	900	120	0.82	0.85	−9.4	3.1	GL(46), MT(8), ILM(11), CPX(21), PL(13), AP(1)	1.16
LS15s[f]	900	120	1.00	1.00	−9.2	3.2	GL, MT, ILM, CPX, PL, AP, ANHY	
LS16s[g]	900	120	0.83	0.85	−9.4	3.1	GL, MT, ILM, CPX, PL, AP, ANHY	
LS33	850	170	1.00	1.00	−10.2	3.2	GL, MT, ILM[e], CPX[e], PL, AP[e], AM	
LS34s[f]	850	170	1.00	1.00	−10.2	3.2	GL, MT, PL, AM, ANHY	
ΔQFM nominal = +1 (at aH_2O=1); P = 200 MPa								
LS17	1000	100	1.00	1.00	−9.8	1.0	GL(85.7), MT(8.9), CPX(5.4)	0.31
LS18	1000	100	0.80	0.83	−9.9	0.8	GL(84.5), MT(8.6), CPX(6.9)	0.17
LS19	1000	100	0.37	0.40	−10.6	0.2	GL(75.8), MT(8.9), CPX(15.3)	0.62
LS20	1000	100	0.31	0.34	−10.7	0.1	GL(46.2), MT(8.0), CPX(25.6), ILM(1.9), PL(18.3)	0.25
LS21	950	120	1.00	1.00	−10.6	1.0	GL(67.3), MT(13.2), CPX(17.8), ILM(1.3), AP(0.4)	0.47
LS22	950	120	0.80	0.83	−10.7	0.8	GL(65.2), MT(13.4), CPX(20.1), ILM(1.0), AP(0.3)	0.50
LS23	950	120	0.45	0.49	−11.2	0.4	GL(39.0), MT(13.8), CPX(25.7), ILM(1.2), PL(19.5), AP(0.8)	0.37
LS24	950	120	0.08	0.09	−12.7	−1.1	Gl[e], Mt[e], Cpx[e], ILM[e], PL[e], AP[e]; -CtS	
LS25s[f]	950	120	1.00	1.00	−10.6	1.0	GL, MT, CPX, ILM, AP, PO	
LS26	900	132	1.00	1.00	−11.4	1.0	GL(52.9), MT(14.8), CPX(22.3), ILM(2.2), PL(6.6), AP(1.2)	0.62
LS27	900	132	0.84	0.87	−11.6	0.9	GL(45.2), MT(14.7), CPX(23.8), ILM(2.1), PL(13.0), AP(1.2)	1.65
LS28s[f]	900	132	1.00	1.00	−11.4	1.0	GL, MT, CPX, ILM, PL, AP, PO	
LS29s[g]	900	132	0.83	0.87	−11.6	0.9	GL, MT, CPX, ILM, PL, AP, PO	
LS30s[f]	900	132	1.00	1.00	−11.4	1.0	GL, MT, CPX, ILM, PL, AP, PO	
LS31	850	168	1.00	1.00	−12.4	1.0	GL, MT, CPX, ILM, PL, AP, AM	

[a] Measured mole fraction of H₂O in the fluid.

[b] Water activity (aH_2O) is calculated from the measured composition of the fluid phase, equation of state for H₂O-CO₂ fluid (Pitzer and Sterner, 1995) and empirical calibration of water activity as a function of fluid composition (Aranovich and Newton, 1999).

[c] Experimental phases: GL = glass, MT = magnetite, ILM = ilmenite, CPX = clinopyroxene, PL = plagioclase, AP = apatite, AM = amphibole, ANHY = anhydrite, PO = pyrrhotite, -CtS = close to solidus. Numbers are proportions of the phases calculated by mass balance; near liquidus experiments with very low melt proportions, as well as experiments with added sulfur are excluded.

[d] Residuals from mass balance calculations.

[e] Phase composition is not determined; phase is identified by EDX.

[f] H₂O-S fluid; water activity is assumed to be not affected by S and equal to unity.

[g] Mixed fluid composed of H₂O, CO₂ and S species; water activity is determined ignoring possible effect of S on H₂O and CO₂ proportions in the fluid (as measured by weight-loss method).

calculated for each experiment using the expression (see also Botcharnikov et al., 2005): $\log fO_2^{capsule} = \log fO_2^{apparent} + 2\log (aH_2O)$, where $\log fO_2^{apparent}$ is the oxygen fugacity which is expected in the system at $aH_2O = 1$. In the case of S-bearing runs, the quantitative determination of fluid composition by the weight-loss method was not possible due to unknown speciation of S in the fluid and very small amounts of free fluid released on freezing and piercing. Hence, for those experiments the possible effect of S on aH_2O and on the redox conditions was ignored, assuming that water activity prevailing in the capsules was close to unity. In the capsules containing H₂O, CO₂ and S, we assumed that the amounts of fluids released on piercing and following heating represent the proportions of CO₂ and H₂O, respectively, owing to a small mass of free S-bearing fluid.

3.3. Attainment of equilibrium

The high volatile diffusivities and fast crystallization kinetics in Fe-rich basaltic to andesitic magmas ensure quick equilibration between silicate melt, fluid and crystallizing mineral phases. Almost all samples (except those few close to the solidus) show evidence of equilibrium by textural and compositional characteristics: (i) The distribution of mineral phases is homogeneous throughout the samples; (ii) the

morphology of the crystals does not indicate any quench crystallization (tails or skeletal forms); (iii) the minerals and glasses have mostly homogeneous compositions; (iv) the crystallization sequence, compositions and proportions of phases follow systematic trends. Fig. 4 shows a backscattered electron images of experimental runs performed at 1050 °C at oxidizing conditions demonstrating the change of phase equilibria as a function of water activity.

3.4. Electron microprobe

The fragments of each sample were mounted in epoxy for electron microprobe analysis. The analyses of the experimental glasses were performed with a Cameca SX100 electron microprobe. Minerals were analyzed with focused beam at 15 kV, 15 nA beam current and counting times for major elements of 10 s. Sodium and potassium were analyzed first with counting times of 5 s to minimize alkali loss. Glasses were measured with a defocused beam of 5 to 20 μm, 4 nA beam current and counting times of 4 s for Na and K, and 8 s for the other elements. In samples with low melt fraction, the microprobe beam was defocused as much as possible. No significant alkali loss (within the uncertainty) was detected using these analytical conditions. Multiple measurements were made for each phase within a sample to minimize possible
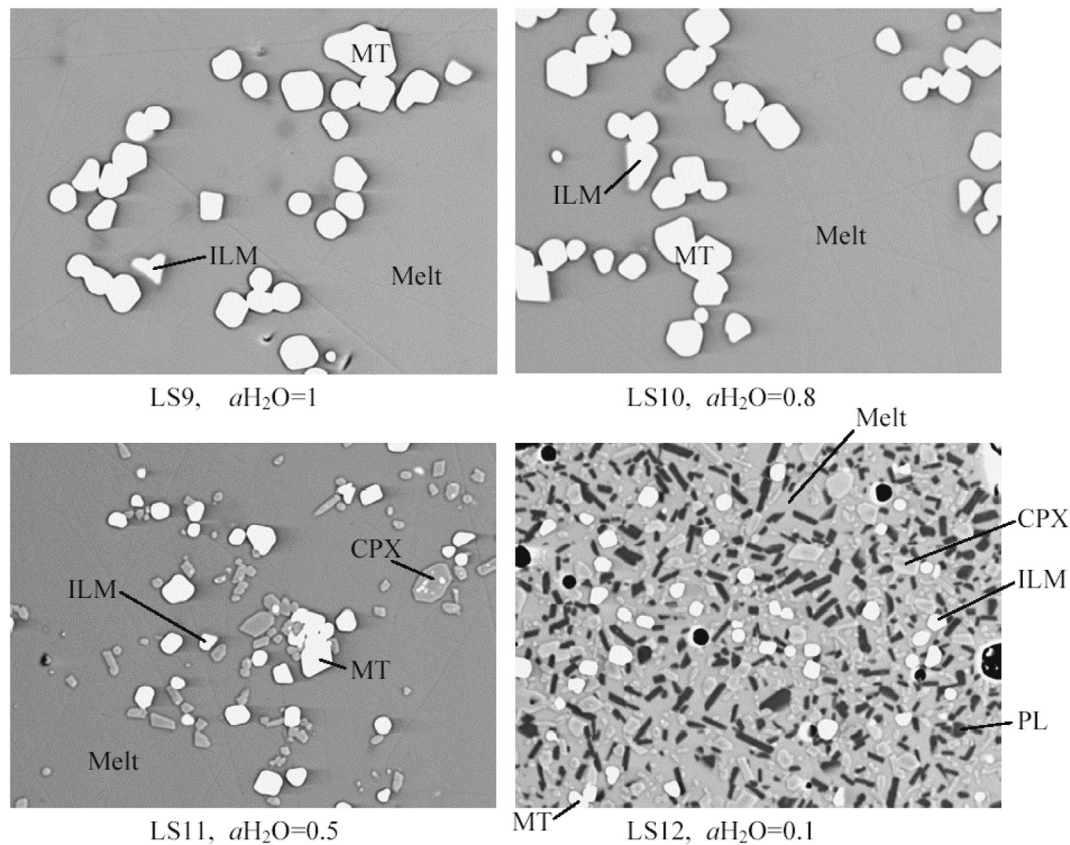
Fig. 4. BSE images of typical experimental products after runs at 1050 °C, QFM + 4. Shown are the mineral phases MT, ILM, CPX, and PL as a function of aH$_2$O surrounded by glass.

analytical errors and check for homogeneity of composition. The results of the electron microprobe analyses of minerals and glasses are presented in Tables 3–11.

The concentrations of S in glasses were determined using defocused beam at 15 kV, 30 nA beam current and counting time of 60 s. Due to low concentrations of S in the glasses the peek search for the Kα shift of the wavelength due to change in S speciation from sulfide to sulfate did not give very good results. Hence, the peak positions close to sulfide and close to sulfate were chosen for the experimental glasses obtained in run series at relatively reducing (i.e., FMQ + 1) and oxidizing (i.e., FMQ + 3.2) conditions. Test measurements at intermediate peak positions changed the results within the analytical uncertainty only. The composition of S-bearing minerals, i.e. anhydrite and pyrrhotite were measured using standard settings (including sulfate S) for silicate analysis in the case of anhydrite, whereas only Fe and S were analyzed in the case of pyrrhotites. The peak position for S was fixed at sulfide S. Pyrite and anhydrite were used as standards for EMPA for sulfide and sulfate S, respectively.

3.5. Determination of water content in experimental glasses

The presence of crystals in the quenched samples limited the amount of analytical methods for determination of H$_2$O concentration in the glass. The H$_2$O content of the glasses was determined using the "by-difference" method (e.g., Devine et al., 1995), i.e. 100% minus analytical total and are presented in Table 3. The analyses were calibrated against basaltic glasses with water contents determined by Karl-Fischer Titration (KFT). Regardless, the precision of the by-difference method is relatively low depending on the counting statistics of the electron microprobe and the typical uncertainty is ≥0.5 wt% H$_2$O. The highest errors are obtained for experimental products with low melt fractions, because glass analyses were only possible with focused or slightly defocused (2–5 μm) microprobe beam.

4. Results

4.1. Stability of phases

The main experimental products are composed of glass (GL), magnetite (MT), ilmenite (ILM), clinopyroxene (CPX), plagioclase (PL), apatite (AP), and amphibole (AM). The phase assemblages are reported in Table 2 and the phase stabilities in terms of water activity and temperature are plotted in Fig. 5. The obtained results show that in this Fe- and Ti-rich late-stage system Fe-Ti-oxides are the liquidus phases at both investigated nominal redox conditions. The oxides are followed by CPX, AP and PL. AP crystallizes at temperatures <1000 °C and its stability is almost independent on aH$_2$O. At reducing conditions, ILM appears at lower temperatures than CPX, whereas MT presumably remains the liquidus phase (Fig. 5). Amphibole crystallizes in experiments at 850°C only, indicating that it becomes stable at temperatures below 900°C, and according to other experimental studies in similar magmatic systems (e.g., Berndt et al., 2005; Botcharnikov et al., 2008; Feig et al., 2006), its stability field should be restricted to conditions with high water activity. Anhydrite (ANHY) and pyrrhotite (PO) are additional mineral phases crystallizing in S-saturated systems at oxidizing and reducing conditions, respectively.

The liquidus and solidus of the system shown in Fig. 5 were extrapolated. For the evaluation of the solidus we investigated the relevant near-solidus experiments carefully with backscattered electron imaging (especially the experiment at 950 °C at nominally dry, and at 850 °C under water-saturated conditions), revealing that the amount of melt in these experiments is very low (<5 vol%), implying that these experiments are slightly above the solidus. Based on these observations and on the experience of evaluating solidus temperatures in similar studies performed earlier using the same experimental technique (e.g., Berndt et al., 2005; Botcharnikov et al., 2008; Feig et al., 2006, 2010) we

Table 3
Major-element compositions of experimental glasses (one-sigma deviation for last digits).

Sample	T, °C	aH₂O	ΔQFM	n	SiO₂	TiO₂	Al₂O₃	FeO*	MnO	MgO	CaO	Na₂O	K₂O	P₂O₅	S	Total	H₂O,[a] wt%
LS9	1050	1.00	3.2	3	51.93 (21)	3.02 (6)	11.83 (18)	9.80 (24)	0.31 (6)	3.99 (1)	9.43 (4)	2.84 (16)	0.31 (4)	0.59 (14)	–	94.07	5.9
LS10	1050	0.81	3.0	5	51.56 (29)	2.97 (7)	11.93 (16)	10.67 (56)	0.23 (11)	3.92 (8)	9.28 (16)	2.87 (12)	0.29 (4)	0.69 (1)	–	94.42	5.6
LS11	1050	0.51	2.6	5	53.41 (57)	2.89 (5)	12.35 (13)	11.57 (19)	0.27 (7)	3.51 (7)	8.94 (20)	2.99 (19)	0.31 (3)	0.70 (5)	–	96.92	3.1
LS12	1050	0.11	1.3	5	64.02 (1.21)	2.14 (11)	11.96 (3)	9.06 (95)	0.19 (8)	1.52 (14)	5.26 (37)	3.84 (9)	0.69 (6)	0.83 (11)	–	99.50	0.5
LS1	1000	1.00	3.2	5	55.07 (57)	2.10 (6)	13.14 (19)	8.15 (24)	0.30 (4)	3.08 (8)	8.87 (30)	3.04 (31)	0.34 (6)	0.81 (4)	–	94.90	5.1
LS2	1000	0.79	3.0	5	55.55 (66)	2.00 (4)	13.54 (17)	8.00 (63)	0.28 (13)	2.87 (12)	8.49 (30)	3.18 (15)	0.32 (4)	0.75 (2)	–	95.00	5.0
LS3	1000	0.44	2.5	5	61.11 (31)	1.59 (9)	13.90 (17)	6.90 (23)	0.28 (8)	1.92 (6)	6.48 (18)	3.94 (29)	0.42 (4)	0.77 (11)	–	97.32	2.7
LS4	1000	0.10	1.2	5	68.39 (1.18)	1.24 (9)	12.60 (36)	6.49 (39)	0.16 (5)	1.09 (28)	4.68 (70)	3.82 (43)	0.76 (8)	0.56 (11)	–	99.79	0.2
LS5	950	1.00	3.2	5	59.54 (25)	1.07 (5)	15.07 (31)	4.32 (25)	0.22 (9)	1.93 (12)	6.84 (43)	3.60 (16)	0.38 (6)	0.44 (4)	–	93.42	6.6
LS6	950	0.82	3.0	5	60.56 (50)	1.04 (7)	15.64 (9)	4.40 (30)	0.23 (5)	1.80 (5)	6.63 (16)	3.73 (19)	0.40 (6)	0.41 (7)	–	94.83	5.2
LS13	900	1.00	3.2	5	65.38 (79)	0.69 (8)	15.18 (19)	3.39 (15)	0.19 (2)	1.10 (4)	4.64 (30)	3.52 (95)	0.48 (3)	0.21 (2)	–	94.79	5.5
LS14	900	0.85	3.1	4	67.58 (82)	0.63 (6)	14.83 (19)	2.89 (25)	0.18 (1)	1.00 (9)	3.96 (16)	3.91 (7)	0.56 (2)	0.19 (3)	–	95.73	4.6
LS15s	900	1.00	3.2	6	64.99 (43)	0.64 (6)	15.62 (25)	3.11 (24)	0.15 (8)	1.44 (11)	4.86 (21)	3.62 (23)	0.47 (7)	0.27 (1)	0.066 (30)	95.23	5.1
LS16s	900	0.85	3.1	7	67.30 (31)	0.62 (5)	14.59 (20)	2.96 (27)	0.19 (1)	1.22 (18)	4.07 (22)	3.30 (26)	0.54 (3)	0.23 (2)	0.046 (6)	95.06	5.3
LS33	850	1.00	3.2	3	66.76 (61)	0.42 (1)	11.01 (7)	2.00 (1)	0.19 (1)	2.05 (12)	4.86 (29)	1.90 (18)	0.51 (2)	1.03 (14)	–	90.74	9.3
LS34s	850	1.00	3.2	4	66.60 (36)	0.43 (7)	11.00 (19)	1.89 (13)	0.20 (8)	2.09 (50)	5.11 (34)	2.09 (21)	0.53 (5)	0.98 (29)	0.012 (3)	90.94	9.1
LS17	1000	1.00	1.0	5	52.81 (35)	2.63 (7)	12.74 (11)	11.80 (46)	0.31 (2)	3.36 (13)	8.59 (22)	2.94 (14)	0.31 (3)	0.77 (3)	–	96.26	4.1
LS18	1000	0.83	0.8	7	52.79 (34)	2.55 (5)	12.85 (22)	12.06 (50)	0.30 (2)	3.14 (12)	8.46 (22)	3.20 (15)	0.31 (3)	0.71 (5)	–	96.38	4.0
LS19	1000	0.40	0.2	6	54.54 (37)	1.99 (8)	14.35 (13)	12.16 (67)	0.29 (2)	2.46 (20)	7.60 (25)	3.58 (26)	0.37 (4)	0.82 (5)	–	98.18	2.5
LS20	1000	0.34	0.1	6	57.83 (30)	1.73 (3)	12.90 (19)	12.75 (42)	0.29 (2)	1.77 (11)	6.49 (15)	3.60 (20)	0.51 (3)	1.12 (5)	–	99.01	1.9
LS21	950	1.00	1.0	5	57.49 (31)	1.31 (9)	15.16 (16)	7.44 (36)	0.25 (1)	1.92 (10)	6.65 (8)	3.62 (24)	0.38 (5)	0.52 (2)	–	94.74	5.6
LS22	950	0.83	0.8	5	58.17 (52)	1.20 (5)	15.37 (25)	7.36 (48)	0.23 (2)	1.84 (7)	6.40 (11)	3.72 (17)	0.37 (3)	0.52 (1)	–	95.19	5.1
LS23	950	0.49	0.4	5	64.37 (51)	0.88 (6)	14.34 (31)	6.36 (28)	0.21 (2)	1.17 (12)	4.61 (10)	4.26 (19)	0.62 (2)	0.41 (2)	–	97.23	3.3
LS25s	950	1.00	1.0	5	56.50 (34)	1.27 (5)	15.11 (23)	7.48 (43)	0.25 (2)	1.96 (6)	6.92 (17)	3.44 (13)	0.39 (3)	0.57 (3)	0.052 (4)	93.95	6.4
LS26	900	1.00	1.0	5	63.31 (38)	0.67 (3)	15.45 (21)	4.71 (29)	0.20 (7)	1.16 (8)	4.72 (16)	4.05 (25)	0.49 (7)	0.16 (15)	–	94.92	5.1
LS27	900	0.87	0.9	5	64.80 (11)	0.62 (1)	15.17 (26)	4.46 (24)	0.25 (5)	1.01 (7)	4.18 (8)	4.08 (37)	0.57 (4)	0.27 (9)	–	95.42	4.6
LS28s	900	1.00	1.0	5	63.26 (54)	0.65 (5)	15.46 (10)	4.99 (19)	0.25 (12)	1.14 (7)	4.59 (8)	3.92 (16)	0.44 (3)	0.28 (3)	0.036 (5)	95.02	5.0
LS29s	900	0.87	0.9	5	65.21 (47)	0.59 (2)	15.01 (23)	4.36 (26)	0.21 (12)	0.99 (6)	4.21 (17)	3.71 (14)	0.50 (1)	0.24 (2)	0.031 (8)	95.07	4.9
LS30s	900	1.00	1.0	6	63.77 (47)	0.65 (4)	15.27 (33)	4.73 (36)	0.22 (6)	1.09 (8)	4.54 (17)	3.80 (22)	0.50 (3)	0.28 (2)	0.038 (8)	94.90	5.1

n – number of analyses.

FeO* is the total content of Fe in the melt.

[a] Water content of the glasses was determined using "by-difference" method.

adjusted the solidus to about ~960 °C for dry and ~ 800 °C for water-saturated conditions, for both oxidizing and reducing conditions.

4.2. Glass compositions

The compositions of experimental glasses are listed in Table 3 and plotted in Fig. 6. The compositional variations of major oxides represent systematic trends with decreasing MgO reflecting the variations in temperature, aH₂O and fO₂. The obtained trends show a good agreement with the experimental data for dry and H₂O-bearing MORB-type ferrobasaltic magmas (Botcharnikov et al., 2008; Toplis and Carroll, 1995).

The evolution of the melt composition with decreasing MgO (MgO as a differentiation parameter) results in significant depletion in Fe and Ti due to the crystallization of oxides (Fig. 6). This effect is pronounced for FeO at oxidizing conditions due to the stabilization of oxides, especially of magnetite. This results in a higher amount of Fe-Ti oxides among the crystallizing minerals. We note that some Fe can be

Table 4
Major-element compositions of experimental clinopyroxenes (one-sigma deviation, last digits).

Sample	T, °C	aH2O	ΔQFM	n	SiO2	TiO2	Al2O3	FeO*	MnO	MgO	CaO	Na2O	K2O	Total	Mg#
LS11	1050	0.51	2.6	1	47.60	2.26	4.63	12.64	0.26	12.48	19.32	0.60	0.02	99.95	64
LS1	1000	1.00	3.2	1	49.79	0.88	2.74	7.87	0.36	14.44	23.41	0.36	0.00	99.86	77
LS2	1000	0.79	3.0	2	50.72 (5)	0.69 (1)	1.96 (3)	7.42 (12)	0.35 (1)	15.29 (9)	23.04 (1)	0.31 (3)	0.02 (1)	99.79	79
LS3	1000	0.44	2.5	5	48.91 (56)	1.05 (3)	3.54 (26)	9.74 (34)	0.53 (4)	13.46 (28)	21.23 (23)	0.41 (4)	0.01 (1)	99.10	71
LS4	1000	0.10	1.2	5	51.19 (1.11)	1.88 (1.22)	3.77 (1.62)	14.26 (99)	0.62 (12)	11.46 (1.17)	16.48 (1.47)	0.64 (28)	0.07 (5)	100.51	59
LS5	950	1.00	3.2	5	49.43 (63)	1.00 (19)	4.15 (87)	8.13 (27)	0.45 (3)	13.62 (78)	22.48 (9)	0.40 (6)	0.02 (1)	99.74	75
LS6	950	0.82	3.0	5	49.17 (34)	0.98 (5)	4.14 (59)	8.27 (28)	0.44 (5)	13.76 (45)	22.32 (44)	0.37 (10)	0.01 (2)	99.53	75
LS7	950	0.38	2.4	1	49.50	1.01	3.06	10.25	0.70	14.22	20.93	0.34	0.02	100.02	71
LS13	900	1.00	3.2	8	49.53 (1.22)	0.88 (26)	3.65 (62)	8.60 (85)	0.62 (6)	14.07 (57)	22.29 (47)	0.41 (3)	0.02 (1)	100.37	74
LS14	900	0.85	3.1	7	50.80 (70)	0.66 (7)	2.82 (47)	8.17 (36)	0.66 (7)	14.77 (37)	22.11 (55)	0.37 (6)	0.02 (1)	100.47	76
LS15s	900	1.00	3.2	9	50.18 (1.13)	0.87 (22)	3.33 (99)	9.22 (21)	0.61 (8)	14.31 (78)	21.24 (49)	0.32 (8)	0.02 (2)	100.34	73
LS16s	900	0.85	3.1	6	52.53 (1.72)	0.76 (38)	2.67 (1.13)	8.80 (89)	0.76 (6)	15.44 (1.09)	19.59 (1.09)	0.36 (10)	0.02 (3)	101.00	76
LS17	1000	1.00	1.0	5	51.43 (54)	0.87 (11)	1.75 (46)	9.09 (45)	0.32 (5)	14.80 (13)	22.44 (27)	0.25 (6)	0.01 (1)	101.01	74
LS18	1000	0.83	0.8	6	50.58 (1.06)	1.15 (41)	2.38 (67)	9.85 (63)	0.36 (5)	14.21 (37)	22.16 (23)	0.32 (6)	0.01 (1)	101.09	72
LS19	1000	0.40	0.2	5	49.47 (1.06)	1.29 (29)	3.14 (43)	12.91 (45)	0.39 (5)	12.64 (20)	20.62 (55)	0.35 (3)	0.02 (1)	100.97	64
LS20	1000	0.34	0.1	6	50.09 (13)	0.79 (5)	1.74 (17)	20.02 (1.56)	0.60 (10)	11.79 (32)	15.46 (1.67)	0.24 (3)	0.00 (1)	100.77	51
LS21	950	1.00	1.0	7	50.19 (1.04)	1.00 (30)	2.96 (1.08)	9.96 (85)	0.42 (3)	13.65 (82)	21.55 (91)	0.27 (3)	0.01 (1)	100.13	71
LS22	950	0.83	0.8	5	49.50 (42)	1.20 (13)	3.96 (39)	10.45 (31)	0.43 (7)	12.63 (25)	21.31 (41)	0.34 (4)	0.03 (1)	99.97	68
LS23	950	0.49	0.4	5	49.44 (84)	0.97 (26)	2.18 (28)	15.87 (85)	0.61 (4)	12.19 (13)	17.63 (60)	0.25 (5)	0.02 (2)	99.42	58
LS25s	950	1.00	1.0	5	49.43 (1.51)	1.21 (31)	3.08 (96)	10.60 (55)	0.40 (3)	13.44 (60)	21.88 (22)	0.31 (6)	0.01 (1)	100.68	69
LS26	900	1.00	1.0	5	49.45 (16)	0.90 (6)	2.98 (15)	11.15 (51)	0.52 (6)	13.55 (14)	20.84 (16)	0.28 (2)	0.01 (1)	99.74	68
LS27	900	0.87	0.9	5	50.30 (81)	0.73 (16)	2.61 (77)	12.32 (1.33)	0.68 (9)	13.80 (66)	19.41 (1.73)	0.30 (10)	0.01 (2)	100.26	67
LS28s	900	1.00	1.0	3	49.50 (28)	0.90 (11)	3.67 (49)	10.73 (38)	0.46 (7)	12.99 (43)	20.63 (15)	0.34 (7)	0.01 (1)	99.38	68
LS29s	900	0.87	0.9	5	49.06 (1.01)	1.00 (50)	2.76 (35)	12.90 (2.67)	0.57 (8)	13.27 (27)	19.59 (1.09)	0.28 (6)	0.01 (1)	99.65	65
LS30s	900	1.00	1.0	4	49.20 (43)	0.88 (13)	2.97 (37)	11.46 (47)	0.53 (5)	13.09 (27)	20.50 (32)	0.30 (6)	0.01 (1)	99.27	67
LS31	850	1.00	1.0	4	49.76 (97)	0.76 (23)	1.86 (47)	15.10 (89)	0.70 (8)	12.77 (41)	18.82 (1.26)	0.26 (8)	0.02 (1)	100.27	60

n – number of analyses.
Mg# = Mg/(Mg + Fe*)*100; on a molar basis with Fe* is total Fe.
FeO* – Fe total as FeO.

also lost due to reaction with the experimental capsule. However, although it is very difficult to assess the amount such Fe lost, the use of Au capsules should minimize Fe loss under relatively oxidizing conditions (i.e., >FMQ + 0.5, Ratajeski and Sisson, 1999) and this was the case for most of our samples (Table 2). The effect of oxide crystallization is responsible for the much higher SiO_2 enrichment in those glasses produced under oxidizing condition than in those produced under more reducing conditions (Fig. 6). Nevertheless, two-thirds of the performed experiments revealed glass compositions of typical oceanic plagiogranites with SiO_2 contents above 60 wt%. Experimental glasses at 850 °C show the highest SiO_2 contents of >73 wt% (normalized), verifying that oceanic plagiogranites very high in SiO_2 can be generated by (extreme) differentiation of MORB (see Section 5.7).

The suppressed stability of PL in systems with high aH_2O (Fig. 5) favours greater increase of Al_2O_3 in the residual melt with magmatic

differentiation compared with the related dry system (e.g. Gaetani et al., 1993; Sisson and Grove, 1993).

4.3. Composition of mineral phases

The compositions of mineral phases are listed in Tables 4–11. Fig. 7a shows the variation of Mg# in clinopyroxene (CPX) with water activity both for oxidizing and reducing conditions, and Fig. 7b shows the An content in plagioclase (PL) as a function of water activity. The effects for both minerals are discussed in the next section. In Fig. 8a and b magnetite-ulvospinel and ilmenite-hematite solid solutions are plotted against ΔFMQ, demonstrating the well-known effect of incorporation of higher ferric iron contents with fO_2 (e.g., Toplis and Carroll, 1995), which is discussed in the next section. Other analyzed minerals of the experimental results are apatites, amphiboles, anhydrites, and

Table 5
Major-element compositions of experimental plagioclases (one-sigma deviation, last digits).

Sample	T, °C	aH2O	ΔQFM	n	SiO2	TiO2	Al2O3	FeO*	MnO	MgO	CaO	Na2O	K2O	Total	An
LS7	950	0.38	2.4	1	55.87	0.15	25.82	1.63	0.02	0.45	11.68	4.49	0.10	100.20	59
LS13	900	1.00	3.2	5	52.38 (1.18)	0.22 (7)	27.64 (1.36)	1.79 (0.35)	0.05 (3)	0.41 (35)	12.76 (1.06)	3.77 (24)	0.09 (2)	99.17	65
LS14	900	0.85	3.1	5	53.00 (61)	0.15 (6)	27.87 (1.16)	1.20 (19)	0.01 (7)	0.20 (11)	12.27 (59)	4.09 (36)	0.08 (4)	98.92	62
LS15s	900	1.00	3.2	10	52.71 (1.43)	0.18 (6)	27.52 (2.15)	1.41 (21)	0.05 (3)	0.52 (52)	12.87 (1.00)	3.62 (44)	0.08 (3)	99.25	66
LS16s	900	0.85	3.1	5	53.75 (42)	0.16 (6)	27.81 (64)	1.26 (14)	0.02 (4)	0.20 (6)	12.06 (37)	4.42 (19)	0.08 (1)	99.95	60
LS33	850	1.00	3.2	3	57.09 (54)	0.44 (12)	25.69 (79)	1.79 (28)	0.05 (3)	0.54 (27)	10.53 (58)	4.70 (63)	0.11 (2)	101.15	55
LS34s	850	1.00	3.2	6	54.09 (1.45)	0.91 (41)	25.23 (1.13)	3.18 (1.29)	0.09 (5)	0.67 (21)	10.87 (49)	4.60 (19)	0.09 (3)	99.74	56
LS20	1000	0.34	0.1	5	56.14 (36)	0.17 (2)	26.87 (35)	1.42 (18)	0.01 (5)	0.15 (7)	10.36 (7)	5.79 (17)	0.10 (2)	101.09	49
LS23	950	0.49	0.4	2	56.31 (1.11)	0.31 (7)	24.50 (85)	2.18 (32)	0.07 (1)	0.34 (6)	10.06 (59)	4.59 (3)	0.15 (4)	98.62	54
LS26	900	1.00	1.0	5	52.84 (1.07)	0.17 (2)	27.70 (96)	1.43 (6)	0.05 (4)	0.32 (6)	12.05 (87)	3.92 (33)	0.08 (2)	98.61	63
LS27	900	0.87	0.9	5	54.26 (1.19)	0.74 (51)	25.42 (2.45)	2.52 (75)	0.06 (4)	0.31 (13)	10.68 (87)	3.90 (52)	0.14 (7)	98.55	60
LS28s	900	1.00	1.0	3	53.69 (1.30)	0.21 (7)	26.16 (82)	1.77 (31)	0.03 (5)	0.68 (48)	11.90 (1.36)	3.80 (36)	0.12 (7)	98.44	63
LS29s	900	0.87	0.9	5	54.46 (1.14)	0.43 (12)	26.82 (1.21)	1.73 (16)	0.07 (6)	0.19 (11)	10.88 (48)	4.76 (53)	0.09 (4)	99.54	55
LS30s	900	1.00	1.0	5	53.04 (1.26)	0.29 (14)	27.01 (1.84)	1.87 (69)	0.08 (4)	0.29 (14)	11.75 (1.15)	3.78 (37)	0.10 (4)	98.36	63
LS31	850	1.00	1.0	3	58.15 (1.28)	0.08 (1)	26.39 (59)	0.76 (7)	0.05 (4)	0.02 (1)	8.18 (77)	7.18 (56)	0.18 (3)	100.99	38

n – number of analyses.
An = Ca/(Ca + Na + K), moles.
FeO* – Fe total as FeO.

Table 6
Major-element compositions of experimental ilmenites (one-sigma deviation for last digits).

Sample	T, °C	aH$_2$O	ΔQFM	n	SiO$_2$	TiO$_2$	Al$_2$O$_3$	FeO*	MnO	MgO	CaO	Na$_2$O	K$_2$O	Total	X$_{ILM}$
LS9	1050	1.00	3.2	3	0.05 (1)	24.23 (16)	0.66 (2)	63.94 (55)	0.13 (4)	2.53 (1)	0.22 (1)	0.02 (2)	0.01 (1)	91.80	0.51
LS10	1050	0.81	3.0	3	0.08 (2)	25.27 (7)	0.62 (1)	63.40 (46)	0.25 (5)	2.59 (6)	0.24 (1)	0.02 (2)	0.01 (1)	92.38	0.53
LS1	1000	1.00	3.2	1	0.08	25.19	0.60	65.35	0.35	2.41	0.17	0.02	0.01	94.15	0.51
LS2	1000	0.79	3.0	1	0.09	26.60	0.64	63.72	0.30	2.43	0.24	0.02	0.00	94.04	0.55
LS3	1000	0.44	2.5	2	0.38 (20)	30.07 (52)	0.76 (1)	59.06 (57)	0.30 (1)	2.17 (9)	0.38 (3)	0.05 (2)	0.02 (1)	93.18	0.63
LS5	950	1.00	3.2	3	0.23 (12)	21.49 (11)	0.80 (4)	65.85 (40)	0.34 (3)	2.00 (4)	0.37 (9)	0.02 (6)	0.01 (1)	91.21	0.45
LS6	950	0.82	3.0	5	0.18 (15)	22.60 (27)	0.83 (7)	65.33 (56)	0.31 (4)	2.00 (5)	0.32 (4)	0.04 (3)	0.00 (1)	91.64	0.47
LS13	900	1.00	3.2	6	0.25 (15)	23.77 (32)	0.69 (3)	66.84 (68)	0.34 (5)	1.80 (7)	0.38 (9)	0.00 (3)	0.01 (1)	94.07	0.48
LS14	900	0.85	3.1	5	0.22 (6)	24.69 (45)	0.64 (3)	66.27 (1.31)	0.37 (7)	1.73 (5)	0.32 (5)	0.01 (5)	0.02 (1)	94.28	0.50
LS15s	900	1.00	3.2	10	0.21 (22)	24.72 (61)	0.71 (4)	66.39 (1.49)	0.36 (4)	2.14 (10)	0.35 (12)	0.01 (3)	0.00 (1)	94.88	0.50
LS16s	900	0.85	3.1	9	0.29 (23)	26.24 (58)	0.67 (3)	63.93 (1.80)	0.39 (3)	2.03 (8)	0.54 (39)	0.04 (5)	0.01 (1)	94.32	0.54
LS20	1000	0.34	0.1	5	0.28 (24)	49.13 (45)	0.30 (7)	47.11 (20)	0.58 (3)	2.21 (2)	0.57 (20)	0.03 (3)	0.01 (1)	100.23	0.97
LS21	950	1.00	1.0	6	0.44 (53)	46.29 (78)	0.33 (1)	48.41 (37)	0.66 (7)	3.40 (10)	0.54 (30)	0.01 (2)	0.01 (1)	100.09	0.92
LS22	950	0.83	0.8	4	0.28 (12)	46.93 (5)	0.37 (3)	48.31 (30)	0.67 (8)	3.30 (6)	0.35 (3)	0.00 (2)	0.01 (1)	100.24	0.93
LS23	950	0.49	0.4	1	0.73	47.36	0.44	44.97	0.59	2.59	0.36	0.09	0.03	97.08	0.97
LS25s	950	1.00	1.0	5	0.17 (11)	46.85 (31)	0.36 (4)	47.92 (28)	0.69 (4)	3.37 (4)	0.35 (4)	0.00 (3)	0.01 (1)	99.76	0.94
LS26	900	1.00	1.0	6	0.20 (10)	47.34 (30)	0.30 (2)	47.70 (9)	0.78 (7)	3.00 (3)	0.37 (8)	0.01 (3)	0.02 (1)	99.68	0.94
LS27	900	0.87	0.9	3	0.64 (21)	47.42 (18)	0.38 (5)	47.30 (27)	0.73 (13)	2.81 (4)	0.46 (4)	0.02 (4)	0.02 (1)	99.80	0.95
LS28s	900	1.00	1.0	3	0.28 (21)	46.99 (27)	0.31 (3)	46.16 (47)	2.90 (4)	0.76 (7)	0.42 (7)	0.01 (3)	0.00 (1)	97.85	0.96
LS29s	900	0.87	0.9	3	0.65 (11)	47.00 (8)	0.39 (6)	46.16 (71)	0.76 (3)	2.86 (6)	0.39 (3)	0.04 (1)	0.01 (1)	98.28	0.96
LS30s	900	1.00	1.0	3	0.25 (6)	46.55 (32)	0.28 (2)	46.77 (34)	0.84 (6)	2.95 (6)	0.44 (11)	0.00 (1)	0.00 (1)	98.15	0.94
LS31	850	1.00	1.0	3	0.19 (6)	47.88 (54)	0.20 (1)	47.07 (38)	1.20 (6)	2.57 (4)	0.49 (10)	0.02 (1)	0.02 (1)	99.65	0.96

FeO* – Fe total as FeO.
n – number of analyses.
X$_{ILM}$ is calculated as X$_{ILM}$ = 2Ti/(Ti + Fe), cations normalized to 2 cations and 3 oxygens.

pyrrhotites, which are listed in Tables 8–11. According to Leake et al. (1997), amphiboles of three samples could be classified as magnesiohornblendes (sample LS33 and LS34s) and pargasite (sample LS31).

The compositional trends of minerals are in agreement with experimental data obtained for the ferrobasaltic system (SC1, SC4) at dry (Toplis and Carroll, 1995) and hydrous conditions (Botcharnikov et al., 2008) (see Section 5.3).

5. Discussion

5.1. Effect of water activity and oxygen fugacity on the mineral phases

Fig. 7a shows that Mg# in clinopyroxene (CPX) is generally higher at more oxidizing conditions than at reducing conditions. This is due to the prevailing oxygen fugacity which controls the Fe^{2+} content and therefore, the Fe^{2+}/Mg ratio of the melt (e.g., Berndt et al., 2005; Feig et al.,

Table 7
Major-element compositions of experimental magnetites (one-sigma deviation for last digits).

Sample	T, °C	aH$_2$O	ΔQFM	n	SiO$_2$	TiO$_2$	Al$_2$O$_3$	FeO*	MnO	MgO	CaO	Na$_2$O	K$_2$O	Total	X$_{MT}$
LS9	1050	1.00	3.2	3	0.09 (3)	5.43 (5)	2.06 (6)	79.10 (24)	0.47 (6)	3.98 (7)	0.19 (3)	0.05 (1)	0.00 (1)	91.40	0.83
LS10	1050	0.81	3.0	3	0.10 (2)	6.00 (2)	2.13 (4)	78.59 (24)	0.53 (3)	3.83 (7)	0.18 (1)	0.03 (4)	0.00 (1)	91.39	0.81
LS11	1050	0.51	2.6	4	0.18 (8)	10.27 (7)	2.74 (2)	74.52 (60)	0.45 (5)	3.48 (10)	0.22 (4)	0.01 (3)	0.01 (1)	91.89	0.67
LS1	1000	1.00	3.2	3	0.12 (1)	5.70 (7)	2.13 (4)	81.20 (46)	0.59 (3)	3.73 (6)	0.22 (1)	0.00 (4)	0.01 (1)	93.68	0.82
LS2	1000	0.79	3.0	1	0.11	6.38	2.3	80.9	0.52	3.51	0.23	0.01	0.02	93.98	0.80
LS3	1000	0.44	2.5	5	0.29 (13)	9.36 (7)	2.78 (3)	76.52 (32)	0.60 (4)	2.74 (1)	0.33 (5)	0.01 (3)	0.01 (1)	92.65	0.70
LS4	1000	0.10	1.2	1	0.40	14.69	2.30	72.29	0.61	1.98	0.28	0.07	0.02	92.66	0.54
LS5	950	1.00	3.2	4	0.38 (26)	3.82 (10)	2.68 (1)	79.27 (46)	0.82 (7)	3.41 (4)	0.35 (11)	0.00 (4)	0.00 (1)	90.79	0.88
LS6	950	0.82	3.0	3	0.22 (9)	5.36 (2.07)	2.74 (13)	78.98 (1.28)	0.77 (9)	3.21 (16)	0.25 (2)	0.04 (5)	0.00 (1)	91.58	0.83
LS13	900	1.00	3.2	8	0.57 (53)	4.43 (9)	2.62 (4)	82.25 (1.10)	0.90 (4)	2.79 (11)	0.54 (25)	0.01 (4)	0.01 (1)	94.18	0.86
LS14	900	0.85	3.1	8	0.58 (48)	4.77 (13)	2.57 (7)	81.91 (1.33)	0.84 (7)	2.59 (4)	0.43 (19)	0.02 (6)	0.00 (1)	93.77	0.85
LS15s	900	1.00	3.2	9	0.33 (16)	4.65 (12)	2.94 (8)	81.81 (1.50)	0.80 (6)	3.16 (6)	0.38 (13)	0.00 (3)	0.01 (1)	94.14	0.85
LS16s	900	0.85	3.1	8	0.34 (20)	5.62 (8)	2.79 (5)	81.62 (1.31)	0.79 (6)	2.82 (7)	0.38 (18)	0.03 (4)	0.00 (1)	94.50	0.82
LS33	850	1.00	3.2	3	2.01 (15)	14.71 (9)	0.95 (9)	72.12 (12)	0.53 (5)	2.23 (6)	1.00 (6)	0.07 (2)	0.02 (1)	93.86	0.54
LS34s	850	1.00	3.2	3	1.21 (22)	14.63 (39)	0.76 (4)	72.91 (46)	0.53 (4)	2.14 (3)	0.76 (11)	0.09 (5)	0.01 (1)	93.04	0.54
LS17	1000	1.00	1.0	17	0.11 (2)	15.43 (13)	2.12 (4)	76.01 (55)	0.54 (6)	2.97 (9)	0.14 (5)	0.01 (4)	0.00 (1)	97.36	0.54
LS18	1000	0.83	0.8	5	0.11 (2)	16.17 (16)	2.21 (3)	75.45 (39)	0.49 (1)	2.91 (9)	0.20 (3)	0.01 (4)	0.01 (1)	97.56	0.52
LS19	1000	0.40	0.2	6	0.15 (3)	19.25 (17)	2.95 (5)	72.48 (29)	0.51 (6)	2.35 (5)	0.26 (4)	0.00 (2)	0.01 (1)	97.97	0.42
LS20	1000	0.34	0.1	5	0.19 (5)	21.63 (20)	2.40 (7)	71.66 (42)	0.51 (3)	1.66 (2)	0.28 (5)	0.00 (1)	0.01 (1)	98.34	0.36
LS21	950	1.00	1.0	6	0.20 (13)	14.66 (27)	2.66 (6)	74.57 (1.05)	0.58 (6)	2.36 (5)	0.27 (7)	0.06 (11)	0.01 (1)	95.37	0.55
LS22	950	0.83	0.8	4	0.13 (2)	15.38 (10)	2.82 (4)	73.06 (31)	0.60 (6)	2.27 (1)	0.20 (4)	0.01 (3)	0.00 (1)	94.43	0.52
LS23	950	0.49	0.4	4	0.63 (15)	17.34 (11)	2.52 (6)	71.46 (28)	0.57 (3)	1.77 (3)	0.50 (7)	0.01 (3)	0.00 (2)	94.82	0.46
LS25s	950	1.00	1.0	8	0.13 (3)	15.13 (9)	2.64 (3)	75.16 (39)	0.61 (4)	2.39 (4)	0.25 (4)	0.00 (3)	0.01 (1)	96.35	0.54
LS26	900	1.00	1.0	5	0.48 (25)	13.64 (39)	2.82 (5)	75.79 (51)	0.67 (4)	2.03 (8)	0.37 (11)	0.05 (4)	0.00 (1)	95.85	0.58
LS27	900	0.87	0.9	2	0.47 (5)	14.07 (4)	2.68 (2)	75.89 (43)	0.69 (1)	1.93 (9)	0.49 (3)	0.02 (5)	0.01 (1)	96.36	0.57
LS28s	900	1.00	1.0	3	0.34 (30)	13.67 (8)	2.80 (6)	74.69 (16)	0.66 (7)	1.90 (7)	0.32 (16)	0.00 (2)	0.00 (1)	94.40	0.58
LS29s	900	0.87	0.9	5	0.52 (30)	14.12 (14)	2.77 (2)	73.92 (77)	0.60 (4)	1.88 (12)	0.41 (14)	0.00 (6)	0.01 (1)	94.29	0.56
LS30s	900	1.00	1.0	5	0.12 (4)	13.48 (24)	2.78 (4)	74.74 (68)	0.62 (4)	1.86 (5)	0.22 (4)	0.02 (4)	0.00 (1)	93.88	0.58
LS31	850	1.00	1.0	3	0.69 (39)	14.59 (27)	2.46 (3)	76.14 (42)	0.86 (4)	1.54 (6)	0.46 (16)	0.07 (1)	0.03 (1)	96.85	0.56

FeO* – Fe total as FeO.
n – number of analyses.
X$_{MT}$ is calculated as X$_{MT}$ = 1 − 3Ti/(Ti + Fe), cations normalized to 3 cations and 4 oxygens.

Table 8
Major-element compositions of experimental apatites (one-sigma deviation, last digits).

Sample	T, °C	aH$_2$O	ΔQFM	n	SiO$_2$	TiO$_2$	Al$_2$O$_3$	FeO*	MnO	MgO	CaO	Na$_2$O	K$_2$O	P$_2$O$_5$	Total
LS5	950	1.00	3.2	2	5.62 (1.37)	0.63 (47)	1.26 (25)	1.49 (31)	0.18 (1)	0.50 (18)	50.21 (3)	0.23 (11)	0.04 (1)	37.59 (47)	97.73
LS13	900	1.00	3.2	3	3.99 (1.95)	0.12 (4)	1.38 (36)	0.87 (14)	0.16 (1)	0.32 (5)	53.02 (1.38)	0.19 (11)	0.04 (2)	39.22 (1.16)	99.31
LS14	900	0.85	3.1	2	2.39 (1.45)	0.06 (1)	0.46 (19)	0.82 (6)	0.22 (6)	0.22 (5)	53.47 (4)	0.07 (1)	0.03 (1)	40.59 (14)	98.32
LS15s	900	1.00	3.2	5	4.55 (2.21)	0.11 (5)	0.96 (55)	1.07 (24)	0.18 (4)	0.39 (9)	52.02 (1.43)	0.29 (10)	0.04 (2)	38.17 (1.52)	98.16
LS16s	900	0.85	3.1	5	3.20 (1.30)	0.10 (2)	0.64 (32)	0.93 (10)	0.19 (3)	0.38 (10)	53.05 (1.16)	0.21 (6)	0.02 (2)	40.63 (1.26)	99.84
LS21	950	1.00	1.0	4	1.41 (47)	0.10 (1)	0.28 (13)	1.27 (4)	0.12 (4)	0.28 (3)	53.56 (23)	0.02 (4)	0.01 (1)	38.41 (30)	95.44
LS22	950	0.83	0.8	2	1.15 (61)	0.09 (3)	0.26 (18)	1.24 (6)	0.14 (2)	0.24 (4)	54.09 (34)	0.06 (4)	0.02 (1)	40.11 (52)	97.41
LS23	950	0.49	0.4	2	1.02 (39)	0.08 (1)	0.18 (4)	1.25 (1)	0.21 (4)	0.18 (1)	54.56 (16)	0.03 (4)	0.01 (1)	40.75 (23)	98.27
LS25s	950	1.00	1.0	8	2.47 (1.40)	0.13 (6)	0.44 (39)	1.36 (15)	0.14 (4)	0.38 (13)	52.92 (1.06)	0.15 (6)	0.02 (1)	40.10 (1.21)	98.49
LS26	900	1.00	1.0	4	1.42 (16)	0.12 (4)	0.28 (9)	1.17 (15)	0.12 (6)	0.18 (2)	53.73 (45)	0.06 (3)	0.01 (1)	38.30 (61)	95.38
LS27	900	0.87	0.9	1	0.90	0.07	0.16	1.10	0.07	0.18	53.74	0.06	0.01	43.73	99.90
LS28s	900	1.00	1.0	7	2.69 (2.04)	0.07 (1)	0.53 (45)	1.04 (15)	0.17 (4)	0.15 (5)	52.17 (1.60)	0.20 (8)	0.03 (2)	40.20 (1.30)	97.80
LS29s	900	0.87	0.9	1	0.81	0.09	0.09	0.92	0.16	0.20	53.61	0.09	0.00	41.20	97.61
LS30s	900	1.00	1.0	2	4.52 (1.69)	0.25 (12)	0.71 (16)	1.60 (27)	0.20 (2)	0.66 (41)	51.35 (1.46)	0.17 (1)	0.03 (1)	37.49 (1.49)	97.14
LS31	850	1.00	1.0	3	0.61 (32)	0.08 (1)	0.18 (16)	1.10 (2)	0.14 (1)	0.10 (1)	54.37 (21)	0.06 (6)	0.02 (2)	33.06 (1.08)	89.74

n – number of analyses.
FeO* – Fe total as FeO.

2006; Toplis and Carroll, 1995). In addition, for both redox conditions, the Mg# in CPX increases with water activity. For instance, at $T =$ 1000 °C for oxidizing conditions, the increase of Mg# in CPX between "nominally dry" and water-saturated runs is ~18 mol% (Table 4). This effect can partly be ascribed to the general increase of Mg# in mafic silicates with water activity at a given temperature (Berndt et al., 2005; Feig et al., 2006, 2010) and partly to the increase of oxygen fugacity, which is a direct consequence of increasing water activities in a H$_2$-buffered system. For this example, the increase in fO$_2$ corresponds to ~2 log units (Table 4) and illustrates the complex relationship between H$_2$O content in the melt and Mg# of mafic minerals in systems where fO$_2$ is controlled by aH$_2$O.

Fig. 7b shows the An content in plagioclase (PL) as a function of water activity. In accord with other studies in hydrous tholeiitic systems (e.g., Berndt et al., 2005; Botcharnikov et al., 2008; Feig et al., 2006; Sisson and Grove, 1993), aH$_2$O increases the An content of PL.

In Fig. 8a and b magnetite-ulvospinel and ilmenite-hematite solid solutions are plotted against ΔFMQ, demonstrating the well-known effect of incorporation of higher ferric iron contents with fO$_2$ (e.g., Toplis and Carroll, 1995). The overall compositional span with fO$_2$ for both solid solutions is ~ 50 mol%. For each solid solution, two clusters of data points are visible, reflecting the two different redox conditions applied in our experiments corresponding to nominal oxygen buffers of log$f$O$_2$ = FMQ + 3.2 and FMQ + 1 (under water-saturated conditions). Thus, the variation of ferric iron within each of the two clusters in both solid solutions is mainly due to the dependence of fO$_2$ on aH$_2$O which is much more pronounced in the magnetite-ulvospinel solid solution (span of 34 mol%) compared to the ilmenite-hematite system (span of 18 mol%).

5.2. Solidus temperature of oceanic gabbros – when did all melt finally solidify?

From seismic refraction data it is known that at fast-spreading ridges and at some slow-spreading ridges, the lower crust behaves as a quite rigid crystal mush under near-solidus conditions. (Crawford and

Webb, 2002; Detrick et al., 1987; Dunn et al., 2000). Thus, the knowledge of the solidus temperature of oceanic gabbros is important for evaluating models of the thermal structure and the physical state of the lower ocean crust.

The phase diagrams obtained in this study allow estimation of solidus temperatures of the late stage system to be ~ 960 °C for dry and ~ 800 °C for water-saturated conditions (see Fig. 5). Thus, the entire interval in a MORB system where crystals and melt may coexist can be estimated from ~ 1230 °C (liquidus of dry primitive MORB, e.g., Almeev et al., 2007) to ~ 800 °C in the case for fractional crystallization of MORB, provided that the late stage processes proceed under hydrous conditions. Strong evidence for hydrous conditions are provided from many late-stage parageneses in oceanic gabbros, since these bear in general amphibole, suggesting that a high water activity prevailed (e.g., Johnson et al., 1994; Merzbacher and Eggler, 1984). The amount of water necessary to stabilize hydrous conditions at low melt fractions can be very low, as roughly estimated in the following. Under a pressure of 100 MPa (corresponding to ~ 3 km depth under ocean ridges when ignoring the water column), the solubility of water in a MORB melt is ~ 3 wt% (Berndt et al., 2002; Hamilton et al., 1964). At a given melt fraction of 0.1, the bulk water content needed for a water activity of unity is 0.3 wt%, a value which can easily be achieved just by advanced differentiation, e.g., after 60% crystallization of anhydrous crystals in a primitive MORB with a primary water content of 0.12 wt% (for fractional crystallization using the COMAGMAT algorithm (Ariskin, 1999); mean average value for primitive MORB according to Sobolev and Chaussidon, 1996).

Coogan et al. (2001) constrained the solidus for gabbros from the MARK area at the Mid-Atlantic Ridge to 860 ± 30 °C, based on coexisting plagioclases and amphiboles interpreted as magmatic and typical late stage parageneses. Koepke et al. (2004) estimated the wet solidus for typical gabbros from slow-spreading crust to values of ~ 870 °C (three different compositions). Moreover, for estimating the wet solidus of mafic rocks of the lower oceanic crust, partial melting experiment on hydrated basaltic material could also be considered. Beard and Lofgren (1991) estimated the wet solidus of a greenstone amphibolite as 875 °C, while France et al. (2010) evaluated the solidus for

Table 9
Major-element compositions of experimental amphiboles (one-sigma deviation, last digits).

Sample	T, °C	aH$_2$O	ΔQFM	name	n	SiO$_2$	TiO$_2$	Al$_2$O$_3$	FeO*	MnO	MgO	CaO	Na$_2$O	K$_2$O	Total	Mg#
LS33	850	1.00	3.2	mghbl	5	48.54 (45)	1.18 (9)	7.50 (29)	8.12 (66)	0.60 (3)	18.31 (43)	12.47 (18)	1.20 (7)	0.06 (1)	98.41	97.3
LS34s	850	1.00	3.2	mghbl	4	49.20 (78)	1.16 (4)	7.33 (12)	8.36 (75)	0.71 (1)	17.68 (20)	12.13 (30)	1.13 (3)	0.06 (1)	97.76	94.7
LS31	850	1.00	1.0	parg	4	39.39 (96)	4.28 (13)	12.33 (55)	16.38 (52)	0.30 (4)	10.01 (59)	11.56 (18)	3.29 (5)	0.55 (3)	98.14	53.5

FeO* – Fe total as FeO.
Mg# = Mg/(Mg + Fe*)*100, on a moler basis.
Name: mghbl – magnesiohornblende; parg – pargasite; based on amphibole formula based on 23 oxygen.
n – number of analyses.

Table 10
Major-element compositions of experimental anhydrites (one-sigma deviation, last digits).

Sample	T, °C	aH₂O	ΔQFM	n	SiO₂	TiO₂	Al₂O₃	FeO*	MnO	MgO	CaO	Na₂O	K₂O	S	Total
LS15s	900	1.00	3.2	6	0.30 (20)	0.05 (1)	0.05 (2)	0.50 (8)	0.04 (2)	0.00 (3)	39.30 (1.07)	0.07 (3)	0.02 (1)	43.20 (1.05)	83.59
LS16s	900	0.85	3.1	4	0.33 (20)	0.05 (3)	0.09 (8)	0.47 (6)	0.06 (15)	0.02 (3)	41.25 (77)	0.02 (1)	0.02 (1)	43.18 (1.42)	85.66
LS34s	850	1.00	3.2	3	0.12 (3)	0.04 (1)	0.03 (1)	0.55 (10)	0.01 (3)	0.03 (1)	39.63 (98)	0.01 (1)	0.02 (1)	48.02 (1.86)	88.50

FeO* – Fe total as FeO.

hydrated sheeted dikes to 830 °C. Our new data allow even lower temperatures for the full freezing of oceanic gabbro. The low solidus temperature is also important for hydrothermal circulation processes operating at high temperatures, since they have the potential to trigger hydrous partial melting. Fluid-triggered partial melting can be expected during high-temperature shearing processes often observed in gabbros from slow-spreading ridges (Koepke et al., 2005a, 2005b), provided a water-rich fluid phase is present and temperatures approach the solidus of the system.

5.3. Comparison of the experimental results with natural trends of oceanic gabbros

For application of our experimental results to natural trends of oceanic gabbro evolution, we chose the co-variation of Mg# in clinopyroxene with plagioclase An content (e.g., Coogan, 2014; Feig et al., 2010), as shown in Fig. 9. Available data sets for natural oceanic gabbros are (mostly obtained by IODP drillings) from SWIR Hole 735B, MARK Leg 153, Mid-Atlantic Ridge Atlantis Massif Hole U1309D, and both Pito Deep and Hess Deep from EPR (Fig. 9). The experimental data obtained in our LS system (as well as those obtained in the dry and hydrous ferrobasaltic systems) form a trend conforming with the gabbro evolution trend from Hess Deep and Pito Deep from the EPR. The trend of gabbros from the Mid-Atlantic Ridge (U1309D and Leg 153) is slightly shifted to lower plagioclase An contents compared to the experimental trend, whereas the evolution trend for the SWIR gabbro is significantly shifted to lower An contents. We note that relevant compositions of highly differentiated rocks are only available for those SWIR gabbros (oxide gabbros from Hole 735B) that contain evolved clinopyroxene coexisting with plagioclase having <30 mol% An contents.

As pointed out by Coogan (2014), the different trends of the natural suites can be explained by different Na contents of the parental melts. MORBs from both Hess and Pito Deeps from EPR have Na₈ contents (which is the basalt Na₂O content corrected for fractionation to 8 wt% MgO, Klein and Langmuir, 1987) of ~ 2.7 wt%, while those from the Atlantis Bank area of SWIR are significantly higher in Na₈ with values around ~ 3.2 wt% (for details see Coogan, 2014). Among the analyses used for the average LS composition (see Section 2, "starting composition") are data from the EPR, the Galapagos Spreading Center, the Juan de Fuca Ridge, and the Mid-Atlantic Ridge, but none from the SWIR, which are characterized by higher Na₈ contents. This may be one reason why the experimental trend is shifted to higher An contents than the SWIR trend. Beside compositional differences between the experimental compositions and natural systems, another difficulty in comparing our experimental trends with those from oceanic gabbros, is that the

gabbros experienced subsolidus elemental exchange during cooling (e.g., Coogan, 2014; Natland and Dick, 2001, 2002). However, low temperature exchange would produce significant zoning at the rims of the primary minerals, especially with respect to the plagioclase, while the cores would be still show the original compositions. So, microprobe analyses of mineral cores would not be affected, neither the related differentiation trends.
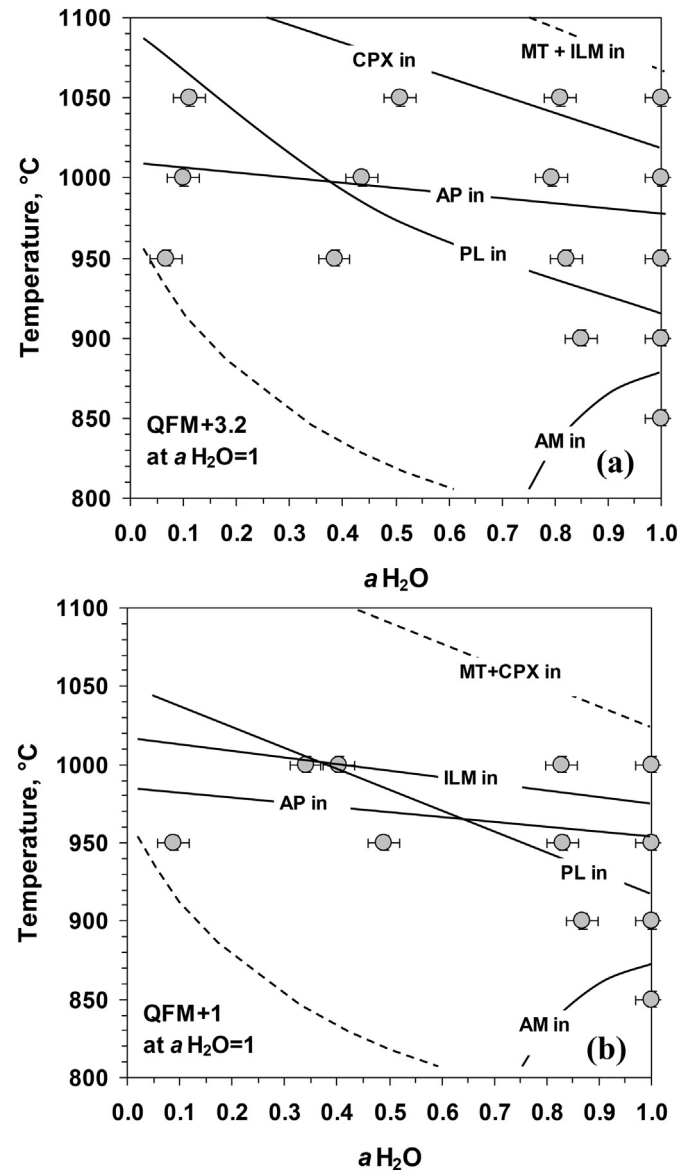

Fig. 5. Phase diagrams illustrating stability fields of mineral assemblages as a function of water activity and temperature. Panels (a) and (b) show data obtained at nominal (at aH₂O = 1) redox conditions corresponding to logfO₂ = FMQ + 3.2 and FMQ + 1, respectively. Solid lines correspond to the saturation curves of minerals, dashed lines correspond to the liquidus and solidus of the system which were extrapolated. For details and abbreviations see text.

Table 11
Compositions of experimental pyrrhotites in wt%.

Sample	T, °C	aH₂O	ΔQFM	n	Fe	S	Total
LS25s	950	1.00	1.0	4	61.76	41.21	102.97
LS28s	900	1.00	1.0	3	60.35	40.83	101.18
LS29s	900	0.87	0.9	4	60.46	40.39	100.85
LS30s	900	1.00	1.0	5	60.88	40.42	101.10
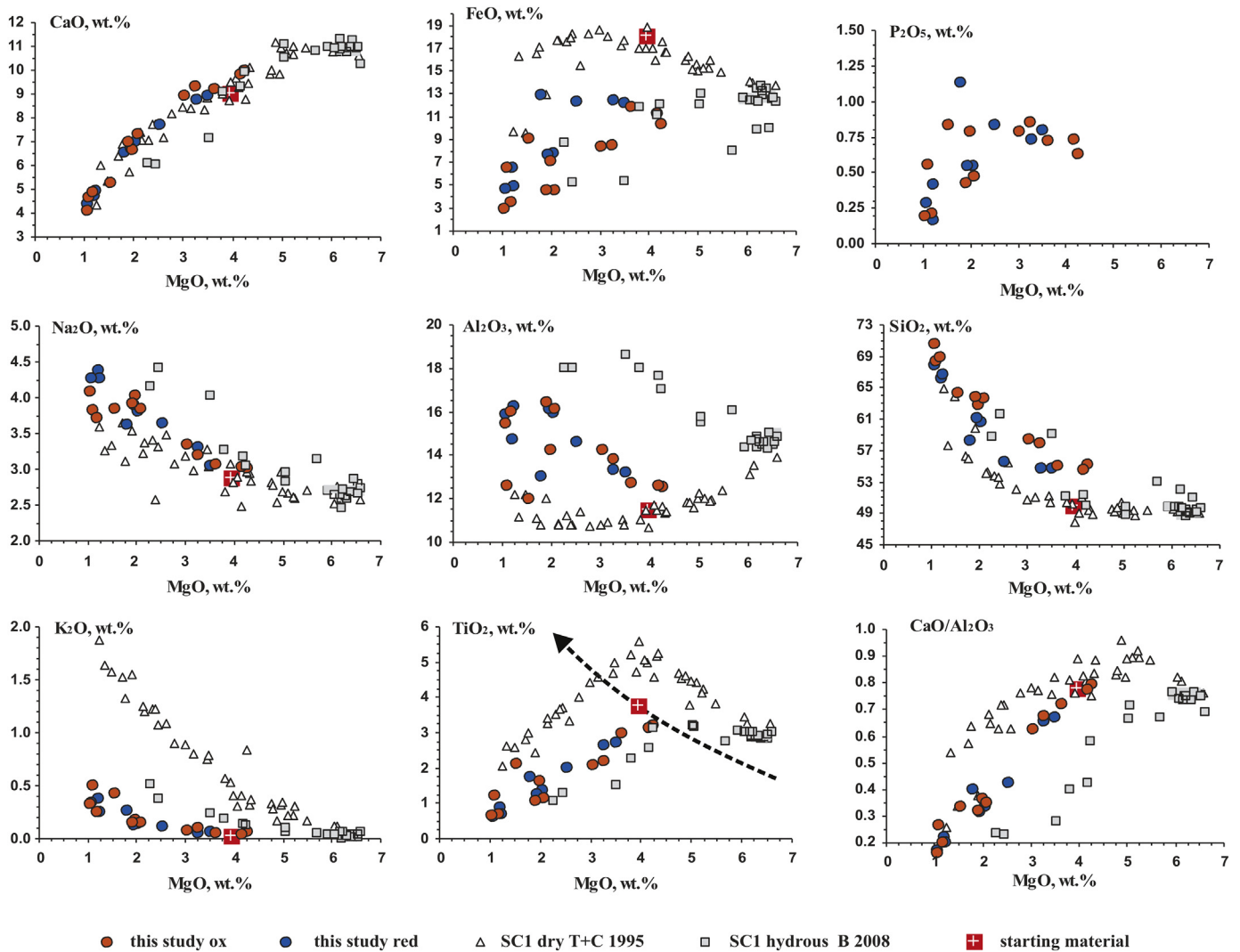
Fig. 6. Compositional evolution of residual melts in crystallization experiments with starting composition "LS". "this study ox": runs at nominal redox conditions at QFM + 4; "this study red" runs at nominal redox conditions at QFM + 1; "SC1 dry T+C 1995": residual glass compositions for dry ferrobasalts (SC1 and SC4 compositions) after Toplis and Carroll (1995); "SC1 hydrous B 2008": residual glass compositions for water-saturated ferrobasalts of SC1 composition after Botcharnikov et al. (2008). "starting material": composition of starting material (late stage melt LS). MgO content of the glasses can be regarded as a magma differentiation index. The arrow in the TiO_2 vs. MgO diagram corresponds to the average liquid line of descent evaluated from four 1-atm studies using natural MORB from mid-ocean ridges as starting material (Dixon and Rutherford, 1979; Juster et al., 1989; Tormey et al., 1987; Walker et al., 1979). The composition of our experimental system LS falls exactly on this trend.

5.4. Formation of evolved abyssal lavas from fast and intermediate spreading ridges

Lavas erupted at mid-oceanic ridges with differentiated compositions (ferrobasalts, dacites) are only known from some sites located at fast and intermediate spreading systems: from the EPR at 9° N, Juan de Fuca Ridge (both in Wanless et al., 2010), GSC (Fornari et al., 1983), and Pacific Antarctic Ridge (Haase et al., 2005). Typical settings for these special abyssal suites are propagating ridge tips at ridge-transform intersections. Extrusive rocks from two of these sites are included in an TiO_2 versus MgO diagram in Fig. 10, together with the experimental results of this study. For the EPR at 9°N, comprehensive geochemical studies imply formation mainly by extensive fractional crystallization of a MORB parent including a minor component of assimilation of partial melts derived from hydrothermally altered mafic rocks, in order to interpret the chlorine contents and oxygen isotopes of these rocks (Wanless et al., 2010). These authors concluded that such evolved lavas are typically located at the ends of ridge segments, with episodic magma supply and enhanced magma/crust interaction. Our results in principle support the fractionation model, by defining a trend which is

similar to the differentiation trend to low MgO values from EPR 9°N, but slightly shifted to higher TiO_2 contents, which is a direct consequence of the high TiO_2 content of the starting compositions LS (Fig. 10). Thus, in combination with other experimental studies in more primitive MORB systems mostly performed at 1 atm (e.g., Juster et al., 1989; Walker et al., 1979) a relatively simple 2-step model for the formation of such evolved abyssal lavas can be formulated. First, primitive MORBs differentiate along the 1 atm cotectic trend to typical ferrobasaltic compositions shown in Fig. 10 by fractionation of olivine, plagioclase, clinopyroxene. This trend continues as long as Fe-Ti oxides are not saturated, which is strongly dependent on the prevailing oxygen fugacity. When such ferrobasaltic magmas are cut off from replenishment by fresh MORB, eventually favoured at segment ends, where magma supply is more episodic, the possibility for further differentiation to highly evolved melts in a second step is given by fractionation of oxides, clinopyroxene, plagioclase and finally amphibole and apatite, as constrained by our experiments. The changing in the trend from ferrobasaltic to the dacitic is probably directly related to the local thermal regime of the ridge segment, i.e. whether the condition for a cut off of replenishment is given (preferentially at segment ends according
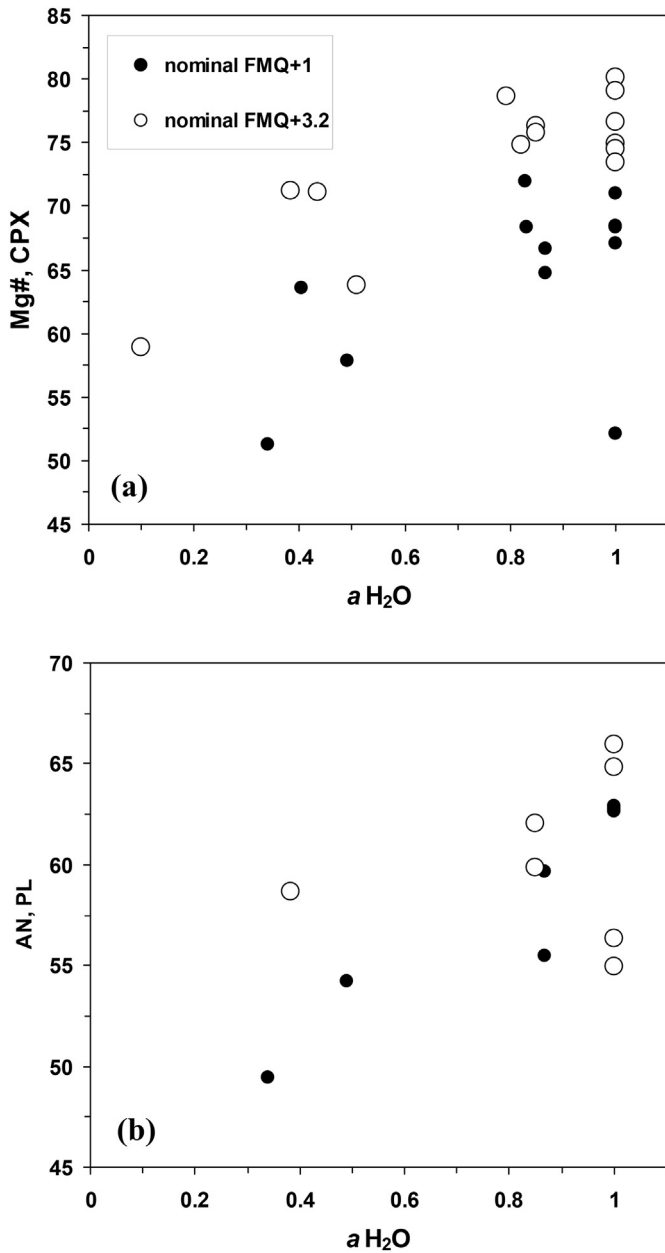
Fig. 7. Compositional variations of experimental CPX (Mg#, a) and PL (An content, b) as a function of water activity and redox conditions.
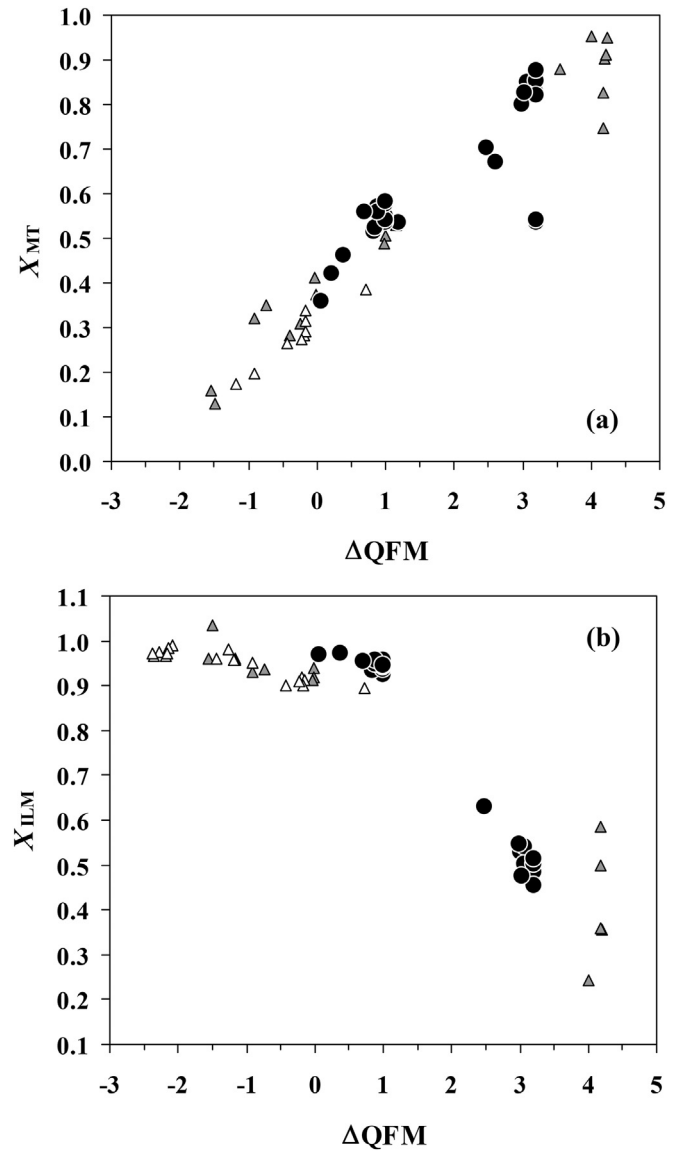

Fig. 8. Compositions of experimental magnetites (a) and ilmenites (b) as a function of redox conditions in the experiments. Black circles are the data from this study, grey triangles are from hydrous ferrobasalt after Botcharnikov et al. (2008), open triangles are oxide compositions from dry ferrobasalts after Toplis and Carroll (1995).

to Wanless et al., 2010). Interestingly, our experimental trend to the dacitic endmember is not significantly influenced by the prevailing redox conditions, as demonstrated in Fig. 10.

For the other suite of highly evolved abyssal lavas presented in Fig. 10, which is from the GSC, the same 2 step differentiation model is implied, but with a "longer" ferrobasaltic trend. Here, a very good correspondence between the natural highly evolved lavas and our results is given, with a kink point located at ~ 4.5 wt% MgO and ~ 3 wt% TiO$_2$ for the natural rock suite in the diagram of Fig. 10, while the corresponding kink point of our experimental trend is given by the LS starting composition, which is at 3.9 wt% MgO and 3.7 wt% TiO$_2$. Although this simple model for the GSC suite seems plausible from Fig. 10, a comprehensive 1 atm experimental study focusing on this situation (Juster et al., 1989) in combination with extensive geochemical study from this region (Fornari et al., 1983; Perfit and Fornari, 1983) demonstrate much more complex genetic relations. Juster et al. (1989) conclude that the strongly evolved liquids of the dacitic trend were formed either by fractionation of MORB-type parents at greater depth under higher pressures

and the presence of a water activities, or by fractionation of parents not directly related to the ferrobasalts. Andesites occurring there are explained by mixing between a basaltic and rhyodacitic liquid. More details can be found in Juster et al. (1989). Nevertheless, the results of our experiments imply that in principle highly evolved abyssal lava suites from fast and intermediate spreading ridges can be explained by a simple 2-step differentiation model.

5.5. Viscosities

In this section we discuss the calculated viscosities of our experimental melts, which could be characterized in the TAS diagram (Total Alkali vs. Silica) as basalt, basaltic andesite, andesite and dacite, in order to estimate the their tendency to erupt. For the calculation, we used the algorithm of Shaw (1972) by applying the EXCEL sheet provided by Winter (2010).
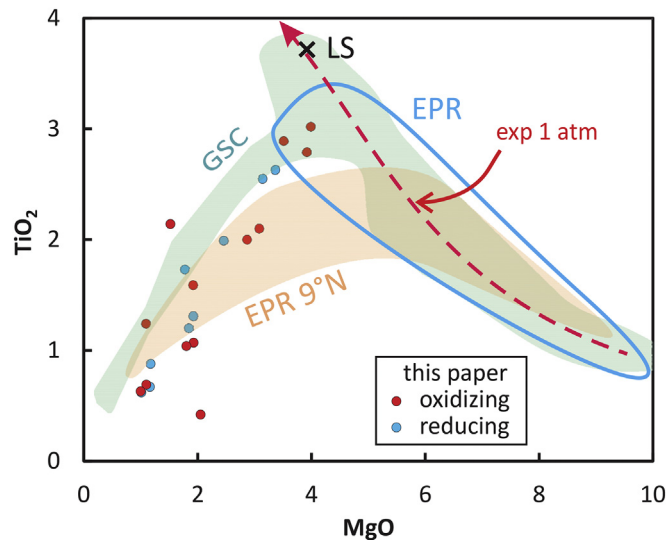
Shaw (1972) showed that the tendency for rhyolite to have high viscosity, and to erupt explosively, is countered by high concentrations of water, and by addition of superheat, with the potential to break down the complex polymers. Since for each of our experimental melts,
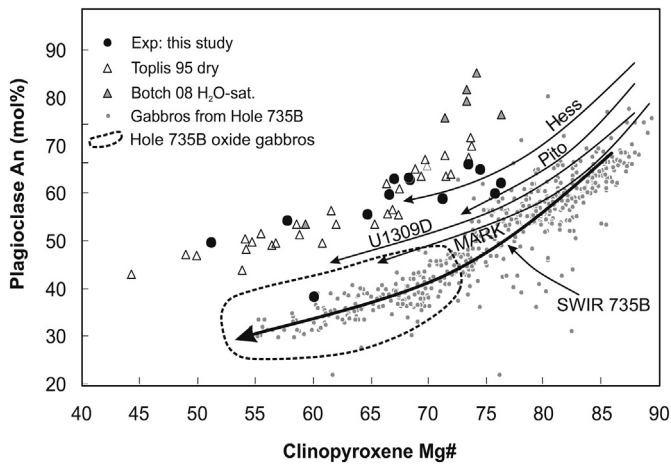
Fig. 9. Plagioclase An content versus Mg# in clinopyroxene: Comparison between experimental data from this study, Toplis and Carroll (1995; dry ferrobasalt with SC1 composition), Botcharnikov et al. (2008; H_2O-saturated ferrobasalt with SC1 composition) and available natural oceanic gabbros from SWIR (Southwest Indian Ridge; Dick et al., 2002; Koepke, unpublished data), MARK (Mid-Atlantic Ridge Kane fracture zone, Coogan et al., 2000; Koepke et al., 2005a; Lissenberg and Dick, 2008), IODP Hole U1309D (Mid-Atlantic Ridge Atlantis massif, Suhr et al., 2008), Pito Deep (East Pacific Rise, Perk et al., 2007), Hess Deep (East Pacific Rise, Dick and Natland, 1996; Miller et al., 1996; Natland and Dick, 1996). For clarity, only the trends are plotted for the natural rocks, except for the gabbros from SWIR, which correspond to the IODP drilling at Hole 735B. The marked field corresponds to highly differentiated gabbros very rich in oxides (oxide gabbros).

temperature, redox condition, and water content is given, viscosities of the melts at run condition were calculated. In addition we assessed the relative effects of water and temperature, and discussed the mobility of different magma types under different conditions at a composite, multiple-intrusion at a slowly spreading ridge.

Fig. 11 presents melt viscosities as functions of MgO and SiO_2 contents, using (1) their experimental temperatures, and calculated dry (no H_2O in the calculation), (2) wet (with H_2O from Table 2, and (3) assuming that the late-stage crystallizing magma body might be invaded by primitive basalt at 1200 °C, adding 150–350° superheat, depending

on the experimental temperature. This amounts to injection of magma into a nearly solid, water-bearing, crystal mush, and might be only a local effect, or a broader one, depending on the extent of the injection. Several basalt dikes, for example, some coarsely crystalline, were encountered in the gabbros of IODP Hole U1473A (MacLeod et al., 2017), located at the Atlantis Bank in the direct neighbourhood of Hole 735B. We are here dealing with intrusive rocks at a repeatedly injected spreading ridge, within which such thermal contrasts, or juxtapositions, can be anticipated. Natland and Dick (2009), for example, described one occurrence of a composite basalt-andesite lava flow from the East Pacific Rise with rhyolite blebs in the andesite that experienced at least 150 °C of superheat during incorporation of the silicic melt into basalt, and its entrainment. They inferred immediate derivation from a subaxial

Fig. 10. TiO_2 versus MgO for natural glasses from fast and intermediate spreading ridges and for experimental melts from this study both for oxidizing and reducing conditions. Included are fields for glasses of differentiated MORB-type suites from GCS and EPR 9° N, as well as for MORB glasses from the EPR excluding those differentiated lavas from EPR 9° N. Included is also the liquid line of descent for typical MORB derived from 1 atm experiments (from Walker et al., 1979 and Juster et al., 1989). The starting composition of the present experimental study, LS, is also included (black cross). For details see text. The compositions of the used natural glasses have been evaluated using the data base PETDB (Lehnert et al., 2000).

Fig. 11. Calculated viscosities vs. SiO_2 (a) and MgO (b) contents. Presented data are: oxi dry, red dry – this study for oxidizing and reducing conditions, calculated for dry conditions; oxi H_2O, red H_2O – this study for oxidizing and reducing conditions, calculated for hydrous conditions with analyzed water contents in melts; oxi H_2O 1200, red H_2O 1200 – this study for oxidizing and reducing conditions, calculated for hydrous conditions with analyzed water contents in melts for a temperature of 1200 °C (assuming superheat); DR 1000, DR 1200 – Fe-rich immiscible melts of Dixon and Rutherford (1979) calculated for the experimental temperature (1000 °C) and for a temperature of 1200 °C (assuming superheat). CG expT, CG 1200 – Fe-rich immiscible melts of Charlier and Grove (2012), calculated for the corresponding experimental temperature and for a temperature of 1200 °C (assuming superheat).

melt lens, with a pod of very differentiated and diverse liquid and that was invaded by basalt, which became their host; mixing occurred beneath a narrow neovolcanic zone near the top of the gabbros.

We have also plotted experimental compositions of Dixon and Rutherford (1979) and Charlier and Grove (2012), both of which succeeded in generating immiscible pairs of high-Fe mafic liquid and silicic melt, but defer discussion of those until the next Section 5.6.

We assume that the viscosities of dry MORB melts represent their window of eruptibility, such that they can flow readily across the sea floor. We assume further that injection of the constituents of oxide gabbros, as represented in experiments mainly by basaltic andesites and andesite, into fabric induced by deformation of a nearly crystalline gabbro mass now atop Atlantis Bank, should have similar or lower viscosities to be mobile. Silicic dikes are represented by dacites in the experimental data, and we also assume that their viscosities during their injection cannot have been much higher than those of basaltic lavas. The question is, how were dry viscosities lowered? These assumptions are somewhat uncertain, within an environment subject to shear, but this is where we start. The results of these evaluation related to viscosities are summarized in the following (see Fig. 11):

(1) All experimental compositions calculated dry are much more viscous, by up to 8 orders of magnitude, than MORB; they cannot erupt as lavas, and can scarcely be mobile in an intrusive environment.

(2) Oxidation state makes no difference to viscosities (closed and open symbols for our experimental melts in Fig. 11 plot atop each other).

(3) Considering water contents estimated for the experimental melts reduces viscosities to the point where some of them match MORB melts.

(4) Adding superheat, assuming a dike or magma injection of 1200 °C, brings a fair number of them, even dacites, down to basalt viscosities.

(5) Dacites, as produced in runs at lower temperatures, are much more viscous than basalts, thus require both water, which was readily available in an amphibole-rich setting, and superheat, for them to be mobile as fluids.

(6) In different terms, lower-MgO, higher-SiO_2, compositions such as dacite are less mobile than near-basaltic compositions at the same temperature and H_2O content, and need all their H_2O and more superheat than basalts to render them mobile.

(7) Differences in viscosity and melt density – the latter much higher in basalt and basaltic andesite, whether or not wet, affect direction of movement – up for dacites, down for differentiated and iron-rich melts, in a gravitational field; oxide-gabbro seams and dacites in the cores atop Atlantis Bank thus tend to diverge, independent of the mode of formation (i.e., by differentiation or by immiscibility; e.g., Natland, 2002).

(8) Addition of both H_2O and superheat to basaltic andesites (<57% SiO2) and even some dacites reduces their viscosities to <10 Pa s, rendering them extremely fluid, on the order of the very low viscosities measured in carbonatites (Dobson et al., 1996). Strictly speaking, the amount of superheat for basaltic andesites need only have been 100–150 °C in order for their viscosities to be lowered to those of basalts. Nevertheless, this may explain the extremely fine scale, narrow width, intimacy of grain-scale penetration, and conformity with, but different degree of deformation from, surrounding rocks, of many seams of oxide gabbro in the Atlantis Bank cores.

5.6. Does silicate liquid immiscibility play a role?

In order to assess the role of liquid immiscibility for the generation of FeO-rich melts leading to oxide gabbros in the oceanic crust, we applied

two sets of experiments attained liquid immiscibility using tholeiitic and alkalic starting basalt compositions. Dixon and Rutherford (1979) carried out 1-atm crystallization experiments on natural MORB glasses from the Galapagos Spreading Center and established that silicate liquid immiscibility exists near temperatures of 1000 °C under dry conditions and at lower oxygen fugacities (tungsten-tungsten oxide, or WWO, buffer) than in our experiments. Immiscible pairs are dacitic and iron-rich glasses with high contents of TiO_2 (up to 7.56%) and P_2O_5 (7.84%). Data from the Fe-rich glasses are included in Fig. 11.

Charlier and Grove (2012) used four different starting compositions falling on basaltic trends relevant for Mull, Iceland, Snake River Plain lavas and for the Sept Iles layered intrusion, where large-scale liquid immiscibility has been recognized. None of these compositions are strict matches for the iron-rich MORB composition relevant for oceanic oxide gabbros as used in our experiments. Their experiments were carried out under dry conditions at 1-atm, using the QFM buffer, at temperatures from 1140 to 936 °C, and resulted in immiscibility for all the different starting composition below 1000–1020 °C. Calculated viscosities of the iron-rich immiscible liquids are also shown in Fig. 11.

All immiscible iron-rich liquids of both Dixon and Rutherford (1979) and Charlier and Grove (2012) have significantly lower SiO_2 than our experimental liquids (Figure visc a). They all also have low viscosities, especially so if they have 160–260 °C of superheat. In both experimental series, immiscibility was obtained without addition of water. Many of the immiscible iron-rich liquids of Charlier and Grove (2012) have very low SiO_2 and MgO contents, and very high FeO, reaching 21.4–32.4, with up to7.14% TiO_2 and 7.91% P_2O_5. Minerals in the iron-rich segregates include ilmenite, magnetite, pigeonite and sodic plagioclase (An28–40 in all but the Iceland experiments; An60–61 in those). These are similar to minerals in oxide gabbros from Hole 735B.

Some of the immiscible Fe-rich liquids fall within the range of MORB eruptive glasses. Equivalent natural compositions might all erupt, although the most iron-rich have not been sampled yet (using PetDb data base). All immiscible compositions likewise are in the eruptive range, although again none, with 19–34% FeO, have been sampled as lavas from mid-ocean ridges. Finally, all immiscible iron-rich liquids subjected to 200° superheat (i.e., by assumed proximal injection of primitive basalt with $T = 1200$ °C) have lower viscosities than typical eruptive basalts, in about the range of liquid carbonatite, and presumably would be very mobile, especially as intrusive liquids under shear. Oxidation state makes little difference, either in our experiments (QFM = 3.2 and 1.0) or QFM for Charlier and Grove (2012) and several log units lower, at WWO, for Dixon and Rutherford (1979). The estimated viscosities plot atop each other. On the other hand, H_2O content in our experiments has a marked effect on lowering viscosities. It is also, apparently, the reason why we did not attain liquid immiscibility and that our liquids follow a nearly calc-alkalic trend (e.g., Charlier and Grove, 2012).

The difficulty with "dry" experimental conditions (Charlier and Grove, 2012; Dixon and Rutherford, 1979), is that the corresponding silicic liquids, even at a terminal, near-solidus stage of fractional crystallization, would still have very high viscosities, even if, after 95% crystallization, they contain 1–2% H2O. Much >200° superheat would be needed to render them as fluid as eruptive basaltic lava. This is even more the case for the truly dry rhyolites of Charlier and Grove (2012). Still, at IODP Holes 735B and U1473A, many oxide gabbros have both euhedral apatite and abundant platy ilmenite-magnetite intergrowths, as in the results of Charlier and Grove (2012), but not all of them. Most are also intergrown with brown paragasitic hornblende. The likelihood, then, is that our wetter experiments more closely approximate the conditions of crystallization of oxide gabbros at Atlantis Bank than the "dry" experiments of Dixon and Rutherford (1979) and Charlier and Grove (2012), and that liquid immiscibility, in this case, did not occur. More detailed comparisons of, e.g., mineral compositions, are required to assess this more fully.

Charlier and Grove (2012) stated that pressure and water promotes early iron depletion, driving the liquid of descent far from the immiscibility field, and both parameters play an important role during the late stage crystallization in the deep fast-spreading crust at pressure conditions between 100 and 200 MPa. It should be noted that examples from natural magmatic systems, where silicate liquid immiscibility played a role, are all related to large gabbroic magma chambers (e.g., Bushveld, Sept Iles, Skaergaard). In contrast, no evidence of this process was recorded from the gabbroic crust of the mid-ocean ridges up to now, which was formed in very small magma chambers (e.g., Vera et al., 1990) under conditions of continuous replenishment, which may prevents an evolution to liquid immiscibility.

5.7. Formation of oceanic plagiogranites in the light of the experimental results

Experimental glasses performed at 850 °C are high in SiO_2, with contents of >73 wt% (normalized to 100%), verifying that oceanic plagiogranites can indeed be generated by (extreme) differentiation of MORB (Fig. 6). As in typical natural oceanic plagiogranites (see review of Koepke et al., 2007), MgO in the high silicic melts is low (~1 wt%), and K_2O high (0.5. to 0.8 wt%). Such a model is supported by other experimental phase equilibria studies in tholeiitic systems, demonstrating that the last melts produced at lowest temperatures are very rich in SiO_2, which could be regarded as source for oceanic plagiogranites (e.g., Berndt et al., 2005; Dixon-Spulber and Rutherford, 1983; Feig et al., 2006). This is also in accord with a model of formation of the felsic veins recorded in IODP Hole 735B of Niu et al. (2002). These authors argued that the veins represent SiO_2-enriched melts as late products of differentiation of MORB magmas with a melt fraction of 10–15%.

On the other hand, for the formation of felsic veins in the gabbro drill core of IODP Hole 735B, Koepke et al. (2007) argued for a model of partial melting of gabbros triggered by the invasion of hydrothermal fluids at temperatures slightly above the gabbro solidus. Based on available experimental data, these authors presented a diagram where TiO_2 versus SiO_2 in melt was plotted including a line representing minimum TiO_2 contents of tholeiitic liquids saturated with iron oxides. Since in tholeiitic systems the evolution to very SiO_2-rich melt compositions can only occur by fractionation of Fe-Ti oxides, it is clear that any SiO_2-enriched liquid generated by differentiation of a MORB parental liquid is expected to plot above the line. As expected, all melt compositions of this study fall above or exactly onto this line, confirming the results found by Koepke et al. (2007). In contrast, melts produced by hydrous partial melting of typical oceanic gabbro fall below this line, because of the very low TiO_2 contents of typical oceanic gabbros which are cumulates. Since most of the analyses from felsic veins of the IODP Hole 735B plot in the TiO_2 vs. SiO_2 diagram below the TiO_2 saturation line, Koepke et al. (2007) argued for hydrous partial melting as formation mode of these veins. This model is also supported when adding the compositions of the felsic veins in the recent drill core of Hole U1473A into the TiO_2 vs. SiO_2 diagram (data in MacLeod et al., 2017). Recently, the dating of zircons from felsic veins of Hole U1473A reveal that some zircons have relatively low formation temperatures showing features typical for hydrothermal formation (Cheadle et al., 2016), implying that the distinction between magmatic and metamorphic processes is blurred, supporting a model of partial melting triggered by hydrothermal activity at temperatures slightly above the solidus.

A third model for the formation of the felsic veins from the IODP Hole 735B is liquid immiscibility (Natland et al., 1991), mainly based on the intimate association between rocks derived from Fe-Ti-rich and silicic melts, and on the experimental study of Dixon and Rutherford (1979). As discussed in the previous Section 5.6, we do not believe that this process played a significant role, responsible for the simultaneous production of oxide gabbro seams and felsic veins in these hydrous rocks. This may depend on the local conditions of the water activity.

5.8. Formation of oxide gabbros at SWIR in the light of the experimental results

In this section we discuss the application of our experimental results to evolved gabbros from the lower ocean crust exposed at the Atlantis Bank at the ultra-slow spreading SWIR, which is by far the best known suite of evolved gabbros from all oceans word-wide, and where three IODP drill cores have been obtained. For the Hole 735B it was reported that 25% of all gabbros involve more differentiated oxide-bearing gabbros (Dick et al., 2000), and for Hole U1473A it was reported that >17% do not represent classical olivine gabbros, but much more evolved oxide-bearing gabbros, which are often enriched in zircon and apatite, confirming their evolved nature (MacLeod et al., 2017). Oceanic gabbros can be regarded as compacted cumulates (average residual melt porosity for Hole 735B gabbros <1.5% according to Natland and Dick, 2001), so it is obvious that the SWIR oxide gabbros correspond more to solidified crystal accumulations than to melts frozen under equilibrium conditions.

In the following we compare the mineral compositions of our experiments with those phases in the Hole 735B gabbros, regarded as mineral assemblages apparently co-crystallized in a magma batch, including domains of oxide gabbro within more primitive gabbro. But, we exclude typical interstitial growth (normally composed only of brown amphibole and Fe-Ti oxides), or analyses from rims of zoned crystals. In Fig. 9, the oxide gabbros follow without any discontinuity the systematic trend formed by troctolites, olivine gabbros and gabbros representing the main part of this trend. We interpret this as continuous crystallization paths as a function of decreasing crystallization temperatures.

In Fig. 9, the corresponding plagioclase/clinopyroxene co-variation trend resulting from our experiments parallels the natural SWIR trend with a shift to higher An contents, which is due to the compositional shift between our experimental system and the SWIR gabbros (see Section 5.3). Thus, Fig. 9 implies that the trend of the natural gabbro indeed corresponds to an evolution path controlled by differentiation of MORB.

Since amphibole crystallized in SWIR oxide gabbros always late it is implied that crystallization started under relatively dry conditions and finished under high water activity, as this is a requirement for amphibole (e.g., Johnson et al., 1994; Merzbacher and Eggler, 1984). The crystallization paths at low aH_2O conditions predicted by our phase relations (Fig. 5) start for oxidizing conditions with co-crystallization of magnetite and ilmenite followed by the saturation of clinopyroxene, plagioclase and apatite. For reducing conditions, crystallization starts with magnetite and clinopyroxene at the liquidus followed by saturation of plagioclase, ilmenite, and apatite. After saturation of plagioclase and apatite, for both redox conditions, co-crystallization of Fe-Ti oxides, clinopyroxene, plagioclase and apatite proceeds over a wide temperature range (70 to 150 °C) both for low and moderate water activities, until the solidus is reached (Fig. 5). This is in accord with the record of crystallization of the SWIR oxide gabbros which are mainly composed of these phases. The presence of apatite during the main stage crystallization in our experiments is reflected by the occurrence of apatite in many oxide-rich gabbros from SWIR, where apatite also occurs as inclusion in plagioclase and clinopyroxene (Meurer and Natland, 2001).

However, our experimental phase assemblage does not include orthopyroxene which is also observed in the SWIR gabbros, both in the main crystallization sequence and in interstitial parageneses. Possible reasons for this may be attributed to compositional differences between our starting material and the natural system, or to higher pressures during the main crystallization of the SWIR gabbro, since it is known that higher pressures stabilize orthopyroxene (e.g., Feig et al., 2006; Villiger et al., 2007). The experiments of Feig et al. (2006), who studied phase equilibria in a MORB-type system at 100, 200 and 300 MPa, showed that with pressure, the orthopyroxene-saturation curve is significantly shifted to higher temperatures (~100 °C for a pressure shift from 100 to 500 MPa). Orthopyroxene could also be stabilized

by higher oxygen fugacities (e.g., Berndt et al., 2005; Feig et al., 2006; Grove and Juster, 1989). Since in a hydrogen-buffered system, the addition of water results in an increase in oxygen fugacity, it is obvious that orthopyroxene-bearing rocks can be generated by simple hydration of a tholeiitic basaltic system. (for further information see discussions in Feig et al., 2006 and Berndt et al., 2005). Another possibility to stabilize orthopyroxene in gabbros of the lower crust is by interaction between primitive MORB melts and peridotite (Coogan et al., 2002).

Alternatively, orthopyroxene in the natural rocks could be a reaction product formed by peritectic reaction between olivine and a percolating evolved melt. Zellmer et al. (2016) investigated such a reaction in natural andesite in detail and found that this reaction is in fact a two-step process: The first step is the dissolution of Mg-rich olivine, which is rate-limited by Mg-Fe interdiffusion at the olivine rim, and the second step is the nucleation and growth of magnesium-rich orthopyroxene preferentially in the melt boundary layer. By investigating in detail textures and mineral compositions in Hole 735B gabbros, Bloomer et al. (1991) found that orthopyroxene-rich domains obviously crystallized in an interval where Mg-rich olivine was reacting out to form low-Ca pyroxenes, and iron-rich olivines were crystallizing as an intergranular phase. From this observation, as we well as from sudden changes in phase assemblages (appearance or disappearance of pigeonite, hypersthene, and olivine), which do not correspond to changes in mineral compositions, these authors imply that orthopyroxene-bearing domains obviously are the product of peritectic reactions between primocrysts and a late, evolved melt. As main reaction, these authors observed that Mg-rich olivine plus an evolved melt form low-Ca pyroxene, with subsequent crystallization of Fe- rich olivine. If this process plays a major role in stabilizing orthopyroxene in the Hole 735B gabbros, it is obvious that our equilibrium crystallization experiments failed to reproduce late-stage orthopyroxene in the natural rocks.

Amphiboles crystallized very late in our experiments (below 900 °C), and only at high water activity, which is consistent with other experimental studies in tholeiitic systems (Berndt et al., 2005; Botcharnikov et al., 2008; Feig et al., 2006, 2010). This is also consistent with the observation in natural SWIR gabbros that amphibole crystallized as a very late phase, often together with Fe-Ti oxides and apatite. Thus, the crystallization of anhydrous phases during the main stage of crystallization drives the water content in the residual melt to higher values, enabling the precipitation of amphibole at the end of differentiation.

From this discussion, oxide gabbro from Hole 735B could be products of equilibrium crystallization of a magma batch in a closed system. However, this simple model is not always supported when investigating textural and compositional details of the oxide gabbro from Hole 735B which provide strong evidence for open system processes. Very often, oxides and other late stage phases such as amphiboles and sulfides are arranged in deformed seams wrapping the primary crystals of the main stage crystallization. Moreover, these late stage phase are often out of equilibrium with the phases of the main stage crystallization, implying that some oxide gabbros do not represented simply cooled closed magma batches. Detailed description on this can be found in Dick et al., (2002), Natland (2002), Natland and Dick (2002), Natland et al. (1991), and Ozawa et al. (1991). Thus, beside equilibrium crystallization of ferrobasaltic melt in accord with our experiments, it is obvious that the gabbro mush was permeated on an intimate, inter-crystalline scale by liquids very rich in iron, titanium, phosphorus and sulfur that probably were added in an open process to their hosts during deformation-assisted intrusion of the countless seams of oxide gabbro. Moreover, it is obvious that these late, highly differentiated melts percolating through a nearly solidified gabbro have the potential to cause peritectic reactions in order to produce orthopyroxene and amphibole (e.g., Bloomer et al., 1991; Coogan et al., 2001). It should be emphasized that the temperature of the gabbro must be above the solidus, otherwise the grain-scale melt migration stops.

6. Conclusions

Crystallization experiments in a late-stage MORB system performed under varying water activities and under redox conditions varying from FMQ − 1.1 to FMQ + 3.2 revealed phase relations and phase compositions which can be used to shed light on the formation of highly evolved abyssal lavas and oxide gabbros in the oceanic crust.

The application of our experimental data to highly evolved abyssal lavas existing exclusively at fast and intermediate spreading ridges, reveal a two-step differentiation model of formation. First, primitive MORBs differentiate along the well-defined 1 atm experimental trend to typical ferrobasaltic compositions by cotectic crystallization of olivine, plagioclase and clinopyroxene. When such ferrobasaltic magmas are cut off from replenishment by fresh MORB, eventually favoured at segment ends, where magma supply is more episodic, the possibility for further differentiation to highly evolved melts in a second step is given by fractionation of oxides, clinopyroxene, plagioclase, apatite and finally amphibole, as constrained by our experiments.

Phase relations obtained in our experiments provide new insights in understanding the formation of oxide gabbros drilled in IODP Hole 735B. Crystallization starts with Fe-Ti oxides, followed by the saturation of clinopyroxene, plagioclase and apatite. Over a wide temperature range (70 to 150 °C) monotonous co-crystallization of Fe-Ti oxides, clinopyroxene, plagioclase and apatite proceeds. This is in accord with the record of crystallization of the SWIR oxide gabbros which are mainly composed of these phases. On the other hand, the detailed petrographic and microanalytical investigations in the Hole 735B gabbro reveal that the magmatic processes forming the numerous oxide seams in the Hole 735B gabbro, were also influenced by open system behavior, assisted by deformative process.

References

Almeev, R., Holtz, F., Koepke, J., Parat, F., Botcharnikov, R., 2007. The effect of H2O on olivine crystallization in MORB: Experimental calibration at 200 MPa. Am. Mineral. 92, 670–674.

Aranovich, L.Y., Newton, R.C., 1999. Experimental determination of CO2-H2O activity-composition relations at 600-1000 degrees C and 6-14 kbar by reversed decarbonation and dehydration reactions. Am. Mineral. 84, 1319–1332.

Ariskin, A.A., 1999. Phase equilibria modeling in igneous petrology: use of COMAGMAT model for simulating fractionation of ferro-basaltic magmas and the genesis of high-alumina basalt. J. Volcanol. Geotherm. Res. 90, 115–162.

Beard, J.S., Lofgren, G.E., 1991. Dehydration melting and water-saturated melting of basaltic and andesitic greenstones and amphibolites at 1, 3, and 6.9 kb. J. Petrol. 32, 365–401.

Berndt, J., Liebske, C., Holtz, F., Freise, M., Nowak, M., Ziegenbein, D., Hurkuck, D., Koepke, J., 2002. A combined rapid-quench and H2-membrane setup for internally heated pressure vessels: description and application for water solubility in basaltic melts. Am. Mineral. 87, 1717–1726.

Berndt, J., Koepke, J., Holtz, F., 2005. An experimental investigation of the influence of water and oxygen fugacity on differentiation of MORB at 200 MPa. J. Petrol. 46, 135–167.

Bezos, A., Humler, E., 2005. The Fe3+/sigma Fe ratios of MORB glasses and their implications for mantle melting. Geochim. Cosmochim. Acta 69, 711–725.

Bloomer, S.H., Meyer, P.S., Dick, H.J.B., Ozawa, K., Natland, J.H., 1991. Textural and mineralogic variations in gabbroic rocks from Hole 735B. In: Von Herzen, R.P., Robinson, P.T., et al. (Eds.), Proceedings ODP, Scientific Results. Ocean Drilling Program Vol. 118. College Station, TX, pp. 21–36.

Botcharnikov, R.E., Koepke, J., Holtz, F., McCammon, C., Wilke, M., 2005. The effect of water activity on the oxidation and structural state of Fe in a ferro-basaltic melt. Geochim. Cosmochim. Acta 69, 5071–5085.

Botcharnikov, R.E., Almeev, R., Koepke, J., Holtz, F., 2008. Phase relations and liquid lines of descent in hydrous ferrobasalt - Implications for the Skaergaard Intrusion and Columbia River Flood Basalts. J. Petrol. 49, 1687–1727.

Brooks, C.K., Nielsen, T.F.D., 1978. Early stages in the differentiationof the Skaergaard magma as revealed by a closely related suite of dike rocks. Lithos 11, 1–14.

Charlier, B., Grove, T.L., 2012. Experiments on liquid immiscibility along tholeiitic liquid lines of descent. Contrib. Mineral. Petrol. 164, 27–44.

Cheadle, M.J., John, B.E., Coble, M.A., Koepke, J., Rioux, M.E., Liu, C.-Z., 2016. IODOP_Expedition_360_Scientists, 2016. The age of IODP Site 1473, Atlantis Bank: Constraints from initial zircon U-Pb dating and geochemistry by SIMS. Abstract OS31D-2052 presented at. Fall Meeting, AGU, San Francisco, Calif (15–19 Dec).

Coogan, L.A., 2014. The lower oceanic crust; 2nd Edition. In: Turekian, K., Holland, H.D. (Eds.), Treatise on Geochemistry. Elsevier, Amsterdam, pp. 497–541.

Coogan, L.A., Kempton, P.D., Saunders, A.D., Norry, M.J., 2000. Melt aggregation within the crust beneath the Mid-Atlantic Ridge: evidence from plagioclase and clinopyroxene major and trace element compositions. Earth Planet. Sci. Lett. 176, 245–257.

Coogan, L.A., Wilson, R.N., Gillis, K.M., MacLeod, C.J., 2001. Near-solidus evolution of oceanic gabbros: Insights from amphibole geochemistry. Geochim. Cosmochim. Acta 65, 4339–4357.

Coogan, L.A., Gillis, K.M., MacLeod, C.J., Thompson, G.M., Hekinian, R., 2002. Petrology and geochemistry of the lower ocean crust formed at the East Pacific Rise and exposed at Hess Deep: a synthesis and new results. Geochem. Geophys. Geosyst., 3 https://doi.org/10.1029/2001GC000230.

Crawford, W.C., Webb, S.C., 2002. Variations in the distribution of magma in the lower crust and at the Moho beneath the East Pacific rise at 9 degrees-10 degrees N. Earth Planet. Sci. Lett. 203, 117–130.

Detrick, R.S., Buhl, P., Vera, E., Mutter, J., Orcutt, J., Madsen, J., Brocher, T., 1987. Multichannel seismic imaging of a crustal magma chamber along the East Pacific rise. Nature 326, 35–41.

Devine, J.D., Gardner, J.E., Brack, H.P., Layne, G.D., Rutherford, M.J., 1995. Comparison of microanalytical methods for estimating H2O contents of silicic volcanic glasses. Am. Mineral. 80, 319–328.

Dick, H.J.B., Natland, J.H., 1996. Late-stage melt evolution and transport in the shallow mantle beneath the East Pacific rise. Proc. ODP Sci. Results 147, 103–134.

Dick, H.J.B., Natland, J.H., Miller, D.J., et al., 1999. Proceedings of the Ocean Drilling Program. Initial Reports, College Station, TX, pp. 1–314.

Dick, H.J.B., Natland, J.H., Alt, J.C., Bach, W., Bideau, D., Gee, J.S., Haggas, S., Hertogen, J.G.H., Hirth, G., Holm, P.M., Ildefonse, B., Iturrino, G.J., John, B.E., Kelley, D.S., Kikawa, E., Kingdon, A., Leroux, P.J., Maeda, J., Meyer, P.S., Miller, D.J., Naslund, H.R., Niu, Y.L., Robinson, P.T., Snow, J., Stephen, R.A., Trimby, P.W., Worm, H.U., Yoshinobu, A., 2000. A long in situ section of the lower ocean crust: results of ODP Leg 176 drilling at the Southwest Indian Ridge. Earth Planet. Sci. Lett. 179, 31–51.

Dick, H.J.B., Ozawa, K., Meyer, P.S., Niu, Y., Robinson, P.T., Constantin, M., Hebert, R., Maeda, J., Natland, J.H., Hirth, J.G., Mackie, S.M., 2002. Primary Silicate Mineral Chemistry of a 1.5-km Section of Very Slow Spreading Lower Ocean Crust: ODP Hole 735B, Southwest Indian Ridge. Proceedings ODP, Scientific results 176, chap. 10. pp. 1–61.

Dixon, S., Rutherford, M.J., 1979. Plagiogranites as late-stage immiscible liquids in ophiolite and mid-oceanic ridge suites: an experimental study. Earth Planet. Sci. Lett. 45, 45–60.

Dixon-Spulber, S., Rutherford, M.J., 1983. The origin of rhyolite and plagiogranite in oceanic crust: an experimental study. J. Petrol. 24, 1–25.

Dobson, P.D., Jones, A.P., Rabe, R., Sekine, T., Kurita, K., Taniguchi, T., Kondon, T., Kato, T., Shimomura, O., Urakawa, S., 1996. The measurement of viscosity and density of carbonate melts at high pressure. Earth Planet. Sci. Lett. 143, 207–215.

Dunn, R.A., Toomey, D.R., Solomon, S.C., 2000. Three-dimensional seismic structure and physical properties of the crust and shallow mantle beneath the East Pacific rise at 9 degrees 30'N. J. Geophys. Res. Solid Earth 105, 23537–23555.

Feig, S., Koepke, J., Snow, J., 2006. Effect of water on tholeiitic basalt phase equilibria: an experimental study under oxidizing conditions. Contrib. Mineral. Petrol. 152, 611–638.

Feig, S., Koepke, J., Snow, J.E., 2010. Effect of oxygen fugacity and water on phase equilibria of a hydrous tholeiitic basalt. Contrib. Mineral. Petrol. 159. https://doi.org/10.1007/s00410-00010-00493-00413.

Fornari, D.J., Perfit, M.R., Malahoff, A., Embley, R.U., 1983. Geochemical studies of abyssal lavas recovered by DSRV Alvin from Eastern Galapagos Rift, Inca Transform, and Ecuador Rift. 1. Major element variations in natural glasses and spatial distribution of lavas. J. Geophys. Res. 88, 10519–10529.

France, L., Koepke, J., Ildefonse, B., Cichy, S., Deschamps, F., 2010. Hydrous partial melting in the sheeted dike complex at fast spreading ridges: experimental and natural observations. Contrib. Mineral. Petrol., 159 https://doi.org/10.1007/s00410-00010-00502-00416.

Gaetani, G.A., Grove, T.L., Bryan, W.B., 1993. The influence of water on the petrogenesis of subduction-related igneous rocks. Nature 365, 332–334.

Grove, T.L., Juster, T.C., 1989. Experimental investigations of low-ca pyroxene stability and olivine pyroxene liquid equilibria at 1-atm in natural basaltic and andesitic liquids. Contrib. Mineral. Petrol. 103, 287–305.

Haase, K.M., Stroncik, N.A., Hekinian, R., Stoffers, P., 2005. Nb-depleted andesites from the Pacific-Antarctic rise as analogs for early continental crust. Geology 33, 921–924.

Hamilton, D.L., Burnham, C.W., Osborn, E.F., 1964. The solubility of water and effects of oxygen fugacity and water content on crystallization in mafic magmas. J. Petrol. 5, 21–39.

Johnson, M.C., Anderson, A.T., Rutherford, M.J., 1994. Pre-eruptive volatile contents of magmas. In: Carroll, M.R., Holloway, J.R. (Eds.), Volatiles in magmas. Mineralogical Society of America, Washington, DC, United States, pp. 281–330.

Juster, T.C., Grove, T.L., Perfit, M.R., 1989. Experimental constraints on the generation of Fe-Ti basalts, andesites, and rhyodacites at the Galapagos spreading Centre, 85°W and 95°W. J. Geophys. Res. 94, 9251–9274.

Klein, E.M., Langmuir, C.H., 1987. Global correlations of ocean ridge basalt chemistry with axial depth and crustal thickness. J. Geophys. Res. Solid Earth Planets 92, 8089–8115.

Koepke, J., Feig, S.T., Snow, J., Freise, M., 2004. Petrogenesis of oceanic plagiogranites by partial melting of gabbros: an experimental study. Contrib. Mineral. Petrol. 146, 414–432.

Koepke, J., Feig, S.T., Snow, J., 2005a. Late-stage magmatic evolution of oceanic gabbros as a result of hydrous partial melting: evidence from the ODP Leg 153 drilling at the Mid-Atlantic Ridge. Geochem. Geophys. Geosyst. 6, 000801–000827 2004GC000805.

Koepke, J., Feig, S.T., Snow, J., 2005b. Hydrous partial melting within the lower oceanic crust. Terra Nova 17, 286–291.

Koepke, J., Berndt, J., Feig, S.T., Holtz, F., 2007. The formation of SiO2-rich melts within the deep oceanic crust by hydrous partial melting of gabbros. Contrib. Mineral. Petrol. 153, 67–84.

Leake, B.E., Woolley, A.R., Birch, W.D., Gilbert, M.C., Grice, J.D., Hawthorne, F.C., Kato, A., Kisch, H.J., Krivovichev, V.G., Linthout, K., Laird, J., Mandarino, J., Maresch, W.V., Nickel, E.H., Rock, N.M.S., Schumacher, J.C., Smith, D.C., Stephenson, N.C.N., Ungaretti, L., Whittaker, E.J.W., Youzhi, G., 1997. Nomenclature of amphiboles - report of the subcommittee on amphiboles of the international mineralogical association commission on new minerals and mineral names. Eur. J. Mineral. 9, 623–651.

Lehnert, K., Su, Y., Langmuir, C.H., Sarbas, B., Nohl, U., 2000. A global geochemical database structure for rocks. Geochem. Geophys. Geosyst. 1 (1999GC000026).

Lissenberg, C.J., Dick, H.J.B., 2008. Melt-rock reaction in the lower oceanic crust and its implications for the genesis of mid-ocean ridge basalt. Earth Planet. Sci. Lett. 271, 311–325.

MacLeod, C.J., Dick, H.J.B., Blum, P., the Expedition 360 Scientists, 2017. Southwest Indian Ridge Lower Crust and Moho. Proceedings of the Integrated Ocean Drilling Program. , p. 360 https://doi.org/10.14379/iodp.proc.14360.14103.12017.

Merzbacher, C., Eggler, D.H., 1984. A magmatic geohygrometer: application to Mount St. Helens and other dacitic magmas. Geology 12, 587–590.

Meurer, W.P., Natland, J.H., 2001. Apatite compositions from oceanic cumulates with implications for the evolution of mid-ocean ridge magmatic systems. J. Volcanol. Geotherm. Res. 110, 281–298.

Miller, D.J., Iturrino, G.J., Christensen, N.I., 1996. Geochemical and petrological constraints on velocity behavior of lower crustal and upper mantle rocks from the fast-spreading ridge at Hess deep. Proc. ODP Sci. Results 147, 477–490.

Miyashiro, A., 1974. Volcanic rock series in island arcs and active continental margins. Am. J. Sci. 274, 321–355.

Natland, J.H., 2002. Magnetic susceptibility as an index of the lithology and composition of gabbros, ODP Leg 176, Hole 735B, Southwest Indian Ridge. In: Natland, J.H., Dick, H.J.B., Miller, D.J., Von Herzen, R.P. (Eds.), Proceedings ODP, Scientific Results. Ocean Drilling Program, College Station, TX, pp. 1–69.

Natland, J.H., Dick, H.J.B., 1996. Melt migration through high-level gabbroic cumulates of the East Pacific rise at Hess deep: the origin of magma lenses and the deep crustal structure of fast-spreading ridges. Proc. ODP Sci. Results 147, 21–58.

Natland, J.H., Dick, H.J.B., 2001. Formation of the lower ocean crust and the crystallization of gabbroic cumulates at a very slowly spreading ridge. J. Volcanol. Geotherm. Res. 110, 191–233.

Natland, J.H., Dick, H.J.B., 2002. Stratigraphy and composition of gabbros drilled at ODP Hole 735B, Southwest Indian Ridge: a synthesis of geochemical data. In: Natland, J.H., Dick, H.J.B., Miller, D.J., Von Herzen, R.P. (Eds.), Proceedings ODP, Scientific Results. Ocean Drilling Program, College Station, TX, pp. 1–69.

Natland, J.H., Dick, H.J.B., 2009. Paired melt lenses at the East Pacific rise and the pattern of melt flow through the gabbroic layer at a fast-spreading ridge. Lithos 112, 73–86.

Natland, J.H., Meyer, P.S., Dick, H.J.B., Bloomer, S.H., 1991. Magmatic oxides and sulfides in gabbroic rocks from ODP Hole 735B and the later development of the liquid line of descent. In: Von Herzen, R.P., Robinson, P.T., et al. (Eds.), Proceedings ODP, Scientific Results. Ocean Drilling Program, College Station, TX, pp. 41–73.

Niu, Y., Gilmore, T., Mackie, S., Greig, A., Bach, W., 2002. Mineral chemistry, whole-rock compositions, and petrogenesis of Leg 176 gabbros: data and discussion. In: Natland, J.H., Dick, H.J.B., Miller, D.J., Von Herzen, R.P. (Eds.), Proceedings ODP, Scientific Results. Ocean Drilling Program, College Station, TX, pp. 1–60.

Ozawa, K., Meyer, P.S., Bloomer, S.H., 1991. Mineralogy and textures of iron-titanium-oxide gabbros from hole 735B. In: Von Herzen, R.P., Robinson, P.T., et al. (Eds.), Proceedings ODP, Scientific Results. Ocean Drilling Program, College Station, TX, pp. 41–73.

Perfit, M.R., Fornari, D.J., 1983. Geochemical studies of abyssal lavas recovered by DSRV Alvin from Eastern Galapagos Rift, Inca transform, and Ecuador Rift:2. Phase chemistry and crystallization history. J. Geophys. Res. 88 (B12), 10530–10550.

Perk, N.W., Coogan, L.A., Karson, J.A., Klein, E.M., Hanna, H.D., 2007. Petrology and geochemistry of primitive lower oceanic crust from Pito deep: implications for the accretion of the lower crust at the Southern East Pacific rise. Contrib. Mineral. Petrol. 154, 575–590.

Pitzer, K.S., Sterner, S.M., 1995. Equations of state valid continuously from zero to extreme pressures with H2O and CO2 as examples. Int. J. Thermophys. 16, 511–518.

Ratajeski, K., Sisson, T.W., 1999. Loss of iron to gold capsules in rock-melting experiments. Am. Mineral. 84, 1521–1527.

Robinson, P.T., Von Herzen, R.P., et al., 1991. Proceedings of the Ocean Drilling Program. Initial Reports, College Station, Texas, p. 826.

Schuessler, J.A., Botcharnikov, R.E., Behrens, H., Misiti, V., Freda, C., 2008. Oxidation state of iron in hydrous phono-tephritic melts. Am. Mineral. 93, 1493–1504.

Shaw, H.R., 1972. Viscosities of magmatic silicate liquids: an empirical method of prediction. Am. J. Sci. 272, 870–893.

Sisson, T.W., Grove, T.L., 1993. Experimental investigations of the role of H2O in calc-alkaline differentiation and subduction zone magmatism. Contrib. Mineral. Petrol. 113, 143–166.

Sobolev, A.V., Chaussidon, M., 1996. H2O concentration in primary melts from supra-sub-duction zones and mid-ocean ridges: implication for H2O storage and recycling in the mantle. Earth Planet. Sci. Lett. 137, 45–55.

Suhr, G., Hellebrand, E., Johnson, K., Brunelli, D., 2008. Stacked gabbro units and interven-ing mantle: A detailed look at a section of IODP Leg 305, Hole U1309D. Geochem. Geophys. Geosyst. 10. https://doi.org/10.1029/2008GC002012.

Teagle, D.A.H., Alt, J.C., Umino, S., Miyashita, S., Banerjee, N.R., Wilson, D.S., the Expedition 309/312 Scientists, 2006. Proceedings Integrated Ocean Drilling Program. , p. 309/312 https://doi.org/10.2204/iodp.proc.309312.302006.

Thy, P., Lesher, C.E., Nielsen, T.F.D., Brooks, C.K., 2006. Experimental constraints on the Skaergaard liquid line of descent. Lithos 92, 154–180.

Toplis, M.J., Carroll, M.R., 1995. An experimental study of the influence of oxygen fugacity on Fe-Ti oxide stability, phase relations, and mineral-melt equilibra in ferro-basaltic systems. J. Petrol. 36, 1137–1170.

Tormey, D.R., Grove, T.L., Bryan, W.B., 1987. Experimental petrology of normal MORB near the Kane Fracture Zone: 22°–25° N, Mid-Atlantic Ridge. Contrib. Mineral. Petrol. 96, 121–139.

Vera, E.E., Mutter, J.C., Buhl, P., Orcutt, J.A., Harding, A.J., Kappus, M.E., Detrick, R.S., Brocher, T.M., 1990. The structure of 0-my to 0.2-my old oceanic crust at 9° N on the East Pacific rise from expanded spread profiles. J. Geophys. Res. Solid Earth Planets 95, 15529–15556.

Villiger, S., Ulmer, P., Muntener, O., 2007. Equilibrium and fractional crystallization exper-iments at 0.7 GPa; the effect of pressure on phase relations and liquid compositions of tholeiitic magmas. J. Petrol. 48, 159–184.

Walker, D., Shibata, T., Delong, S.E., 1979. Abyssal tholeiites from the oceanographer frac-ture Zone II, phase equilibria and mixing. Contrib. Mineral. Petrol. 70, 111–125.

Wanless, V.D., Perfit, M.R., Ridley, W.I., Klein, E., 2010. Dacite petrogenesis on mid-ocean ridges: evidence for oceanic crustal melting and assimilation. J. Petrol. 51, 2377–2410.

Winter, J.D., 2010. Principals of Igneous and Metamorphic Petrology. New York (Prentice Hall).

Zellmer, G.F., Sakamoto, N., Matsuda, N., Iizuka, Y., Moebis, A., Yurimoto, H., 2016. On progress and rate of the peritectic reaction Fo + SiO_2 —> En in natural andesitic arc magmas. Geochim. Cosmochim. Acta 185, 383–393.